

# Geochemistry, Geophysics, Geosystems



### RESEARCH ARTICLE

10.1029/2021GC010291

### **Key Points:**

- We directly compare zircon (U-Th)/ He data and thermal maturation of organic matter from within and outside the Punchbowl fault, California
- Zircon (U-Th)/He dates are not completely reset and models indicate coseismic temperatures were likely ≤725–800°C
- Temperatures inferred from zircon (U-Th)/He data are consistent with biomarker results and suggest temperature rise varied in space and time

### **Supporting Information:**

Supporting Information may be found in the online version of this article.

### Correspondence to:

E. M. Armstrong, ema.armstrong@usu.edu

### Citation:

Armstrong, E. M., Ault, A. K., Bradbury, K. K., Savage, H. M., Polissar, P. J., & Thomson, S. N. (2022). A multiproxy approach using Zircon (U-Th)/
He thermochronometry and biomarker thermal maturity to robustly capture earthquake temperature rise along the Punchbowl fault, California.

Geochemistry, Geophysics, Geosystems, 23, e2021GC010291. https://doi.org/10.1029/2021GC010291

Received 3 DEC 2021 Accepted 3 MAR 2022

### **Author Contributions:**

Conceptualization: A. K. Ault, H. M. Savage, P. J. Polissar Formal analysis: E. M. Armstrong, H. M. Savage, P. J. Polissar, S. N. Thomson Funding acquisition: E. M. Armstrong, A. K. Ault, H. M. Savage, P. J. Polissar Investigation: E. M. Armstrong, K. K. Bradbury

© 2022 The Authors.

This is an open access article under the terms of the Creative Commons Attribution-NonCommercial License, which permits use, distribution and reproduction in any medium, provided the original work is properly cited and is not used for commercial purposes.

# A Multi-Proxy Approach Using Zircon (U-Th)/He Thermochronometry and Biomarker Thermal Maturity to Robustly Capture Earthquake Temperature Rise Along the Punchbowl Fault, California

E. M. Armstrong<sup>1</sup>, A. K. Ault<sup>1</sup>, K. K. Bradbury<sup>1</sup>, H. M. Savage<sup>2</sup>, P. J. Polissar<sup>2</sup>, and S. N. Thomson<sup>3</sup>

<sup>1</sup>Department of Geosciences, Utah State University, Logan, UT, USA, <sup>2</sup>Department of Earth and Planetary Sciences, University of California, Santa Cruz, CA, USA, <sup>3</sup>Department of Geosciences, University of Arizona, Tucson, AZ, USA

**Abstract** During an earthquake, work done to overcome fault friction is dissipated as heat. Coseismic temperature rise, critical for identifying and constraining the magnitude of past earthquakes, is difficult to accurately quantify. To address this issue, we compare two temperature-sensitive geochemical systems, zircon (U-Th)/He (ZHe) thermochronometry and thermal maturity of organic matter (biomarkers), which respond to short-duration, high temperatures. Models of prior biomarker data from the Punchbowl fault (PF), CA, indicate coseismic temperatures of ~465-1,065°C in the principal slip zone (PSZ; Savage & Polissar, 2019, https:// doi.org/10.1029/2019gc008225) depending on prescribed thickness of the deforming zone. We resampled two PF sample sites and acquired high-spatial resolution ZHe data (n = 45 individual analyses) from the PSZ and fault core gouge, together with adjacent crystalline basement and Punchbowl Formation rocks. Results define a positive ZHe date-effective U (eU) trend from ~10 to 60 Ma and ~20-700 ppm eU with a plateau at ~65 Ma at >700 ppm eU. This pattern suggests the PSZ and fault core gouge share a similar thermal history to material outside the PF. Individual apatite (U-Th)/He dates (n = 5) from an undeformed Punchbowl Formation sample are ~4 Ma for grains with ~30–150 ppm eU, implying rapid cooling and exhumation at that time due to PF activity. Zircon damage-diffusivity relationships inform a suite of numerical models that collectively bracket coseismic temperatures on the PF to <725–800°C for 90% He loss. Results support general compatibility between ZHe and biomarker-derived temperature rise estimates, and spatio-temporal variability in coseismic temperatures along the PF.

Plain Language Summary Earthquakes produce heat along faults from friction created as blocks of rock slide past each other. Identifying evidence of and quantifying these temperatures can pinpoint past earthquakes along faults and help us understand the physics of earthquakes. It is difficult to measure temperatures of modern earthquakes because the fault may be hot for less than a minute far below Earth's surface. Here we compare data from two techniques, heat-induced chemical changes in organic materials (biomarkers) and geochemical changes in minerals (zircon (U-Th)/He analysis), which are sensitive to short-lived, high temperatures. We apply zircon (U-Th)/He analysis to samples within and away from the Punchbowl fault, a strike slip fault in southern California and an ancient strand of the San Andreas fault system, where prior biomarker data showed evidence of past earthquake temperature rise in material within the fault. Zircon (U-Th)/He results, along with numerical models, reveal that earthquake temperatures were likely less than 725–800°C within the fault, similar to previous temperature estimates. Data also suggest earthquake temperatures may have been variable in space and time. Our work illustrates the agreement between these two geochemical methods and that this dual-approach can quantify earthquake-generated heat in other fault zones worldwide.

### 1. Introduction

Earthquakes dissipate most frictional energy as heat (Kanamori & Brodsky, 2001; Lachenbruch & McGarr, 1990; McGarr, 1999). Slip localization during earthquake propagation can yield temperature rise along discrete (µm-to cm-thick) layers where heat generation outpaces conductive heat dissipation (Platt et al., 2014, 2015; Rice, 2006; Rice et al., 2014). Temperature rise is an important aspect of earthquake mechanics as higher temperatures activate dynamic weakening mechanisms that promote continued earthquake rupture propagation (Di Toro et al., 2011; Goldsby & Tullis, 2011; Reches & Lockner, 2010; Wibberley & Shimamoto, 2005). Quantifying

ARMSTRONG ET AL. 1 of 20



Methodology: E. M. Armstrong, A. K. Ault
Project Administration: A. K. Ault, H. M. Savage
Resources: A. K. Ault
Supervision: A. K. Ault, K. K. Bradbury
Visualization: E. M. Armstrong
Writing – original draft: E. M.
Armstrong
Writing – review & editing: E. M.
Armstrong, A. K. Ault, K. K. Bradbury, H. M. Savage, P. J. Polissar, S. N.

and mapping high temperatures along exhumed faults can identify past earthquakes and inform in situ earthquake physics, frictional energy dissipation, and fault slip history.

Fault rock chemistry and textures are used to estimate subsolidus fault slip temperatures (e.g., Rowe & Griffith, 2015, and references therein). These textures and mineral reactions include decarbonation (Collettini et al., 2013; McIntosh et al., 1990), thermal decomposition of clays (Kameda et al., 2011), serpentine dehydration (Kohli et al., 2011), hematite oxidation state transformations and texture-targeted noble gas thermochronometry (Ault et al., 2015; Calzolari et al., 2020; Evans et al., 2014; McDermott et al., 2017), and thermal maturation of organic matter (biomarkers; Savage & Polissar, 2019). Biomarkers are organic molecules in sedimentary rocks that alter as a function of temperature, and certain biomarkers are sensitive to transient temperature rise (Polissar et al., 2011; Rabinowitz et al., 2017; Savage & Polissar, 2019; Savage et al., 2014; Sheppard et al., 2015).

Analogous to organic material alteration, thermochronometry of minerals in fault zones track a fault's thermal history. Traditionally, minerals growing in fault zones are targeted to constrain the timing of fault slip using radioisotopic systems (e.g., Nuriel et al., 2012; Nuriel et al., 2019; van der Pluijm et al., 2001). But low-temperature thermochronometry of minerals entrained or precipitated in fault rocks, a technique that is nominally used to constrain cooling due to tectonic or erosional exhumation (Armstrong et al., 2003; Ehlers et al., 2003; Reiners, 2005; and many others), can record the timing and temperatures of fault slip (Ault, 2020). For example, fission-track annealing and He diffusion kinetics respond to short-duration, high temperature thermal pulses associated with coseismic frictional heating in either a bulk layer or at surface asperities during seismic slip (Ault et al., 2015; Calzolari et al., 2020; McDermott et al., 2017; Murakami et al., 2006; Tagami, 2012), although not all seismogenic faults exhibit thermochronometric evidence of temperature rise (d'Alessio et al., 2003). Zircon (U-Th)/He (ZHe) thermochronometry is a low-temperature radioisotopic system with a broad temperature sensitivity that varies depending on intragrain U and Th concentrations and resulting radiation damage accumulation in different zircon grains over their thermal history (Guenthner et al., 2013). This system is sensitive to short-duration, high temperatures and has been used to identify wildfires (Mitchell & Reiners, 2003) and shear heating (Maino et al., 2015).

A multi-method comparison of fault slip paleotemperature proxies with different kinetics is useful for robustly capturing coseismic temperatures and overcoming individual method limitations. Here, we compare biomarkers and ZHe thermochronometry to refine peak coseismic temperatures along the Punchbowl fault (PF), CA. The PF is an ancient, exhumed strand of the San Andreas fault (SAF), with a localized, discrete principal slip zone (PSZ), that developed during past earthquakes (Chester & Chester, 1998; Chester & Logan, 1987). Recent biomarker analyses show evidence of concentrated friction-generated heat along the PSZ of the PF during fault slip (Savage & Polissar, 2019). Models of temperature rise in the PSZ using biomarker reaction kinetics indicate ~465–1,065°C for a slip zone half-width of 50 μm to 10 mm slipping at 1 m/s.

We resampled a subset of PF sample sites of Savage and Polissar (2019) exposed at Devil's Punchbowl Natural Area (Figure 1). We compare existing biomarker data with newly acquired ZHe thermochronometry data from a site with a well-defined PSZ and a second location characterized by a broader zone of fault core gouge, as well as from the adjacent crystalline basement and Punchbowl Formation (Fm) protoliths. We also acquired apatite (U-Th)/He (AHe) and apatite fission-track (AFT) thermochronometry for comparison with our ZHe results. We use thermal history modeling of material outside the PF to constrain the background thermal history of material within the PF. A suite of numerical modeling approaches is then used to constrain maximum coseismic temperatures along the PF and we compare these results with prior work.

# 2. Background

### 2.1. Geologic Framework

The PF is an inactive, abandoned strand of the SAF (Chester & Chester, 1998). The PF is parallel to and located ~3.5 km southwest of the SAF, adjacent to the San Gabriel Mountain section of the Transverse Ranges (Figure 1). At our study site in Devil's Punchbowl Natural Area, two strands define the PF. We focus on the northern strand, which is more continuous and easier to identify (Chester & Chester, 1998). Here, the PF juxtaposes Miocene-Pliocene Punchbowl Fm to the northeast against Mesozoic and older gneissic crystalline basement to the southwest (Figure 1). Basement rocks are variably mapped as Precambrian crystalline basement, Mesozoic and older crystalline rock, or Mesozoic Wilson Diorite (Barth, 1990; Chester & Chester, 1998; Coffey, 2015; Coffey, Ingersoll,

ARMSTRONG ET AL. 2 of 20

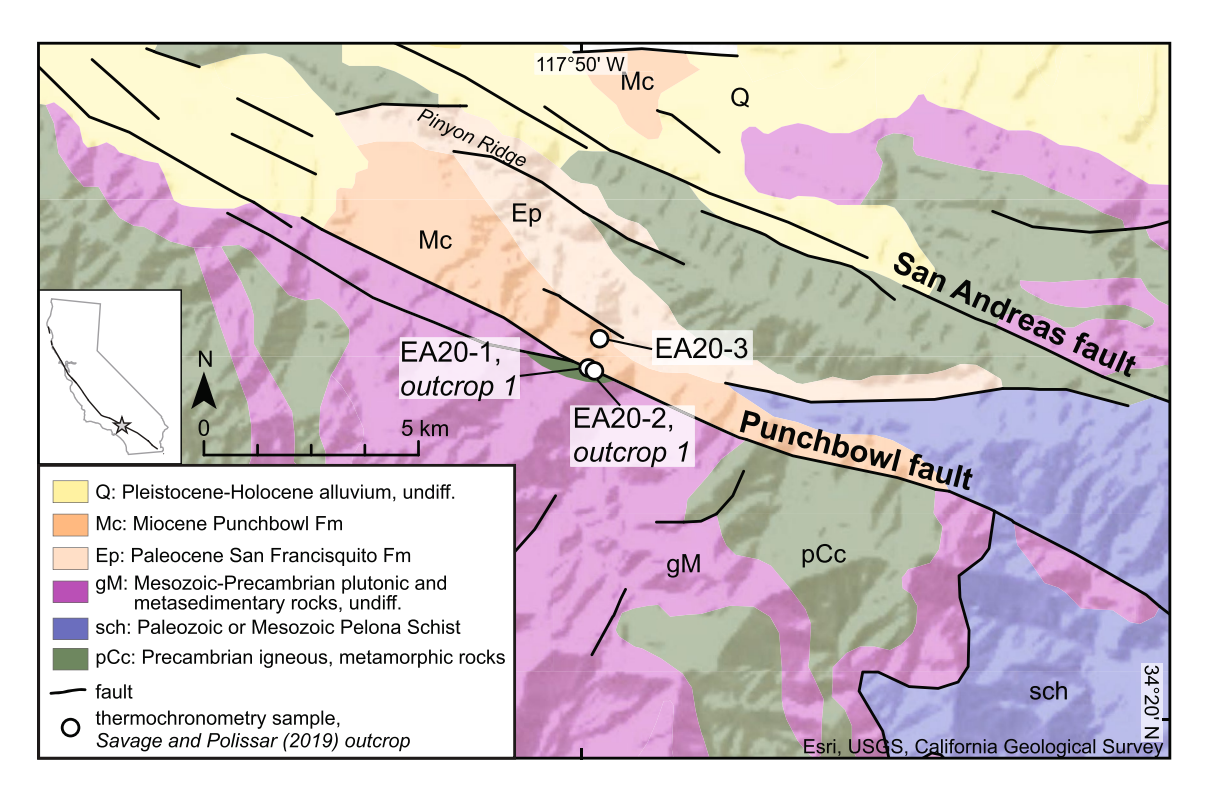


**Figure 1.** Simplified geologic map modified from California Geological Survey overlain on a digital elevation model showing the Punchbowl fault in the Devil's Punchbowl Natural Area and San Andreas fault, San Gabriel Mountains, CA. Biomarker (Savage & Polissar, 2019) and new thermochronometry (this study) site locations are shown

& Schmitt, 2019). Although some crystalline basement rocks in the San Gabriel Mountains have well-constrained crystallization ages, the age of the gneiss at our specific sample sites is unknown.

The Punchbowl Fm is a syntectonic sedimentary deposit in the Punchbowl block, an inferred pull-apart basin formed by offset along the PF (Chester & Chester, 1998). The Punchbowl Fm is 1,500 m-thick, unconformably overlies the Paleogene San Francisquito Fm, and comprises fluvial to alluvial conglomerate and sandstone that were deposited ~12.5–8.5 Ma (Liu, 1990; Woodburne, 1975). The basal unit of the Punchbowl Fm is a conglomerate that is distinct from the main Punchbowl Fm unit and is cut by, and overlies, the PF (Chester & Chester, 1998). Detrital zircon U-Pb age spectra from the Punchbowl Fm include peaks at ~70–100 Ma, ~150–160 Ma, ~210–260 Ma, ~1,400 Ma, and ~1,700 Ma (Hoyt et al., 2018; Ingersoll et al., 2013). Prior work suggests the provenance for zircon grains in the Punchbowl Fm is the distal Mojave region located northeast of the present location of the Punchbowl Fm (Barth et al., 1997; Coffey, Ingersoll, & Schmitt, 2019; Meisling & Alexander, 1993; Woodburne, 1975).

The PF was likely seismogenic because it is an adjacent strand of the SAF, which produces earthquakes, and the PF exhibits textural and biomarker evidence of friction-generated heat that accompanies coseismic slip (Chester & Chester, 1998; Savage & Polissar, 2019). The PF accommodated more than 40 km of strike-slip displacement from Miocene through Pleistocene time, but the exact timing of slip and seismogenesis is poorly constrained (Chester & Chester, 1998; Chester et al., 1993). Faulting may have occurred in two phases, with half of the displacement before deposition of the Punchbowl Fm and the remaining displacement in the Plio-Pleistocene (~6-1 Ma) following deposition of the entire Punchbowl Fm (Chester & Chester, 1998; Meisling & Alexander, 1993; Woodburne, 1975). Alternatively, all of the slip may have occurred in the last ~5 Ma (Coffey, 2015; Coffey, Ingersoll, & Schmitt, 2019; Schulz & Evans, 1998, 2000).

Apatite fission track cooling dates from nearby basement rocks are  $\sim$ 9 Ma and  $\sim$ 4 Ma (Blythe et al., 2000), supporting exhumation associated with PF activity. Limited unpublished AFT dates from the Punchbowl Fm are  $\sim$ 15–7 Ma (Kirschner, 2004). AFT dates and an initial suite of biomarker analyses from large samples both suggest  $\sim$ 2–4 km of exhumation for present-day fault exposures (Blythe et al., 2000; Chester, 1983; Chester &

ARMSTRONG ET AL. 3 of 20



Logan, 1986; Polissar et al., 2011; Savage & Polissar, 2019). During this exhumation, on-going deformation and/or fluid-rock interaction along the PF may have overprinted textural and mineralogical evidence of coseismic temperature rise.

In the vicinity of Devil's Punchbowl Natural Area, the PF architecture is well characterized with a fault core and broader damage zone (Chester & Logan, 1986; Schulz & Evans, 1998, 2000). The PF is an archetypal example of a fault with a thin slip zone formed by strain localization (Chester & Chester, 1998; Chester & Logan, 1987). A PSZ is observed in the center of the fault core of some PF exposures, delineated by a narrow (<1 cm-wide) layer of clayey fault gouge, with a distinctively different color (brown to yellow) than the adjacent fault core (Chester & Logan, 1986; Savage & Polissar, 2019). The fault core surrounding the PSZ is ~0.15–0.25 m wide, olive-black (on the basement side) or dark yellow to brown (on the Punchbowl side) ultracataclasite (Chester & Chester, 1998; Chester & Logan, 1986; Chester et al., 2005). The material comprising the ultracataclasite on either side of the PSZ is derived from its respective, adjacent host rock (Chester & Chester, 1998; Savage & Polissar, 2019). Ultracataclasite and the PSZ comprise highly comminuted quartz and feldspar, as well as smectite, reflecting later alteration and fluid-rock interaction during exhumation from seismogenic depths (Chester & Chester, 1998). The broader fault damage zone is ~140 m wide (Chester & Logan, 1986; Dor et al., 2006; Schulz & Evans, 1998, 2000; Wilson et al., 2003).

### 2.2. Biomarker Evidence for Coseismic Temperature Rise on the Punchbowl Fault

Biomarker maturity patterns support friction-generated temperature rise in the PF PSZ (Savage & Polissar, 2019). Biomarkers are organic molecules, derived from the remains of organisms, that are present in sedimentary rocks, and whose molecular composition alters as a function of temperature (Peters et al., 2007; Sheppard et al., 2012, 2015). The relative alteration indexes of different organic molecules, such as methylphenanthrenes, increase with increasing thermal alteration (Polissar et al., 2011; Radke, 1988; Sheppard et al., 2015). The kinetics of temperature-dependent reactions associated with a particular index are used to quantify temperature rise. Although biomarker reactions are cumulative over all heating events experienced by a fault, biomarker alteration is highly non-linear with respect to temperature and therefore the maximum temperature dominates the signal (Coffey, Savage, et al., 2019). Biomarkers also do not have retrograde reactions (Coffey, Savage, et al., 2019; Peters et al., 2007). The index relevant to the present study, MPI-4, is sensitive to short-duration, high temperatures associated with earthquakes (Polissar et al., 2011; Savage & Polissar, 2019; Savage et al., 2018; Sheppard et al., 2015).

Initial biomarker analyses from the PF used large samples that did not specifically isolate different components of the PF such as the PSZ and showed no differential heating between the fault core and off-fault samples (Polissar et al., 2011). Biomarker thermal alteration constrained peak burial temperatures in the Punchbowl Fm and material in the fault core derived from this unit to ~110°C (Polissar et al., 2011). Recent work leveraged new approaches for analyzing smaller volume samples, making it possible to subsample discrete, thin layers like the PSZ (Savage & Polissar, 2019). MPI-4 data patterns indicate some samples achieved higher peak temperatures than others, with the highest MPI-4 found in the PSZ. In addition, the population of samples from the PSZ and the brown ultracataclasite are generally more thermally mature than the black ultracataclasite and undeformed Punchbowl Fm. This indicates that the brown ultracataclasite is made of reworked and transported PSZs that experienced coseismic temperature rise, as had been previously proposed based on structural analysis (Chester & Chester, 1998; Savage & Polissar, 2019). Modeled peak temperatures from MPI-4 values in the PSZ are ~465–620°C from a 10 mm slip zone and ~815–1,065°C commensurate with a 50 μm slip zone (Savage & Polissar, 2019).

### 2.3. Zircon (U-Th)/He Thermochronometry

The ZHe system is traditionally used to decipher slow, low-temperature processes of rocks transiting the upper  $\sim$ 8 km of the crust, such as tectonic or erosional exhumation (Reiners, 2005; and others). The ZHe closure temperature ( $T_c$ ) is  $\sim$ 25–225°C, assuming a 10°C/Ma cooling rate and depending on accumulated radiation damage in a zircon crystal (Ginster et al., 2019; Guenthner et al., 2013). AHe and AFT thermochronometry can provide complementary thermal history information (e.g., Armstrong et al., 2003; Ehlers & Farley, 2003). The AHe and

ARMSTRONG ET AL. 4 of 20



AFT  $T_c$  are ~30–90°C and ~60–120°C, respectively, assuming a 10°C/Ma cooling rate and variable accumulated damage for AHe and grain chemistry for AFT (Flowers et al., 2009; Gallagher, 1995; Gautheron et al., 2009).

Aside from temperature and time, the main control on the ZHe T<sub>c</sub> is radiation damage accumulation in a zircon crystal (Guenthner et al., 2013; Ketcham et al., 2013). Accumulated radiation damage is a function of a grain's U and Th content and thermal history (Guenthner et al., 2013). Metamict, or radiation-damaged, zircon grains are easily identified with a stereoscope, appearing brown-opaque in plane-polarized light (Ault et al., 2018). Metamictization develops because actinide decay disrupts the crystal lattice, and it anneals (i.e., is recovered) as a function of increasing temperature (Holland & Gottfried, 1955; Nasdala et al., 1995; Woodhead et al., 1991). Provided grains share a common thermal history, a grain's eU (effective uranium, eU = [U] + 0.235\*[Th]) serves as a proxy for radiation damage. Accumulated damage controls He diffusion, and thus a grain's T<sub>c</sub> and ZHe date. At low eU and accumulated damage, zircon is more retentive with respect to He, and the T<sub>c</sub> increases with increasing damage. Above a percolation threshold where damage becomes interconnected, zircon He retentivity and T<sub>c</sub> decrease (Guenthner et al., 2013; Ketcham et al., 2013; Nasdala et al., 2004). Patterns between ZHe date and eU of multiple grains within a single sample or grains that share a common thermal history develop because of the relationship between damage, He retentivity, and the thermal history. For example, grains that experienced protracted thermal histories may yield a positive and/or negative ZHe date-eU trend (Ault et al., 2018; DeLucia et al., 2018; Flowers et al., 2020; Guenthner et al., 2013; Johnson et al., 2017; Orme et al., 2016; Powell et al., 2016). Uniform single grain dates across a wide range of eU values, or a ZHe date-eU "pediment" or "plateau", may reflect a phase of rapid cooling at that time (e.g., Ault et al., 2018; DeLucia et al., 2018).

Zircon diffusion kinetics are also sensitive to short-duration, high temperature pulses (Mitchell & Reiners, 2003; Reiners, 2009). The temperatures required to induce substantive He loss from zircon crystals over a range of geologic conditions are inversely and logarithmically proportional to the duration of heating over a range of geologic conditions (Reiners, 2009). Depending on the accumulation of radiation damage and the conditions of fault slip, the ZHe system may be thermally reset by coseismic friction-generated heat. For example, ZHe results from fault rocks might yield uniform dates across a range of eU values, reflecting complete thermal resetting (i.e., He loss) of all grains at the time of the earthquake if the event occurred at depths and background temperatures lower than the nominal closure temperature at slower cooling rates. Here we compare ZHe and biomarker data, two systems with different reaction kinetics, from the same fault rocks to refine the range of peak temperatures achieved during fault slip.

# 3. Thermochronometry Sampling Approach and Analytical Methods

Samples were collected in Devil's Punchbowl Natural Area, CA, where semi-continuous exposures of the PF are preserved (Figures 1, 2a, and 2b; Table S1 in Supporting Information S1). We targeted *Outcrop 1* of Savage and Polissar (2019) because this location exhibits biomarker evidence for increased temperature rise along the PSZ and the structural and microtextural analysis of our selected site are well-characterized (Chester & Chester, 1998; Chester & Logan, 1986, 1987; Chester et al., 1993).

We collected samples in two high-spatial resolution transects perpendicular to the trace of the PF separated by  $\sim 10$  m along strike, sites EA20-1 and EA20-2 (Figures 2a, 2b and 3a, and 3b). At each site, we sampled crystalline basement, Punchbowl Fm, and PF fault materials over a distance of  $\sim 15$  cm. The basement rocks form a sharp, sub-vertical, contact with the fault core gouge (Figures 2a and 2b), mirroring the overall orientation of the PF ( $\sim 294/70$ ; Chester & Logan, 1987). Fault rocks are highly comminuted and friable. Individual layers of gouge were isolated with a large pocketknife and collected with a flat trowel. Basement and Punchbowl Fm samples were removed with a hammer and chisel.

The structural architecture of the fault zone is distinct at each site. At site EA20-1, we sub-sampled fault rocks based on previous characterization (Chester & Chester, 1998; Savage & Polissar, 2019) because sub-units could be distinguished by color (Figure 2a). Here, fault zone domains include: basement-side (black) ultracataclasite (1A), the PSZ (1B), and Punchbowl Fm-side (brown) ultracataclasite (1D). The fault architecture at site EA20-2 was comparatively homogeneous and lacked obvious sub-domains, so we collected a single fault core gouge sample (hereinafter referred to as "gouge"; sample 2B; Figure 2b). Crystalline basement samples (1C and 2A; Figures 2a and 2b) were slabbed with a water-cooled saw perpendicular to the fault core contact at 1-cm intervals to create subsamples at <1 cm, 1–2 cm and >2 cm away from the fault zone interface (samples 1C-1, 1C-2, 1C-3,

ARMSTRONG ET AL. 5 of 20



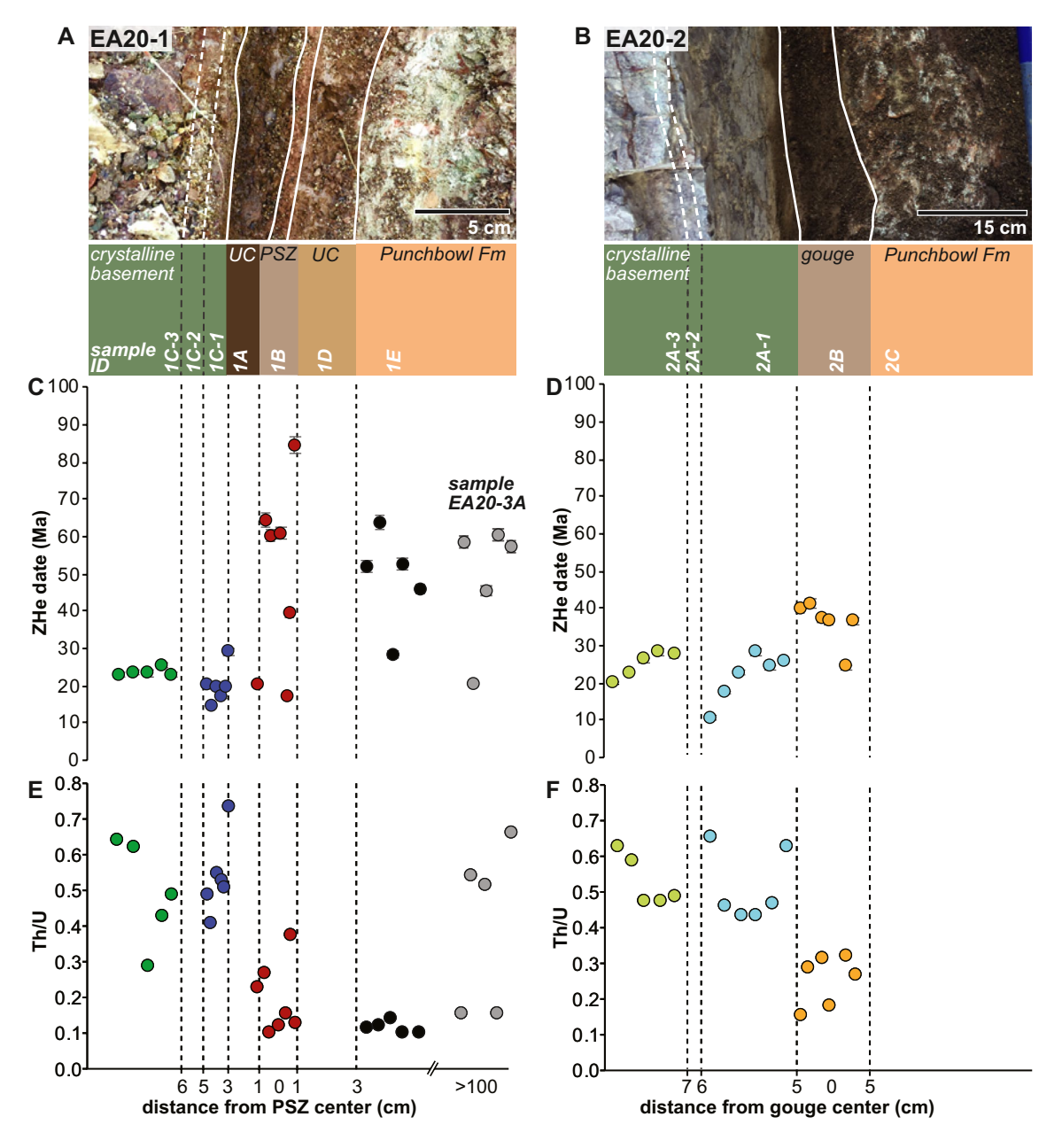


Figure 2. Field photos and schematic diagrams of sample transects at sites (a) EA20-1 and (b) EA20-2; specific sample IDs noted. (c), (d) Individual zircon (U-Th)/He (ZHe) dates and (e), (f) corresponding Th/U ratios for samples at sites EA20-1 and EA20-2, as well as sample EA20-3A as a function of distance from the center of the fault zone. Date error bars are  $2\sigma$  analytical uncertainty. UC = ultracataclasite; PSZ = principal slip zone; Fm = formation.

and 2A-1, 2A-2, and 2A-3, respectively). Sample 3A consists of undeformed Punchbowl Fm  $\sim$ 100 m north of the PF (Figure 1).

Accessory phases were isolated using standard crushing methods, including mortar and pestle for more friable samples, hand washing, and magnetic separation techniques in the Utah State University Mineral Microscopy and Spectroscopy Lab (M<sup>2</sup>SL). Heavy liquid separation and a second and final magnetic separation was performed at Zirchron, LLC. We targeted a subset of samples for ZHe analysis including the PSZ (1B), gouge (2B), basement (1C-1, 1C-3, 2A-1, 2A-3), and Punchbowl Fm (1E, 3A), because of inferences about the presence and absence of friction-generated heat from biomarker data (Savage & Polissar, 2019). Each sample yielded limited, whole zircon grains and numerous apatite fragments, but whole apatite grains required for (U-Th)/He analysis were only

ARMSTRONG ET AL. 6 of 20



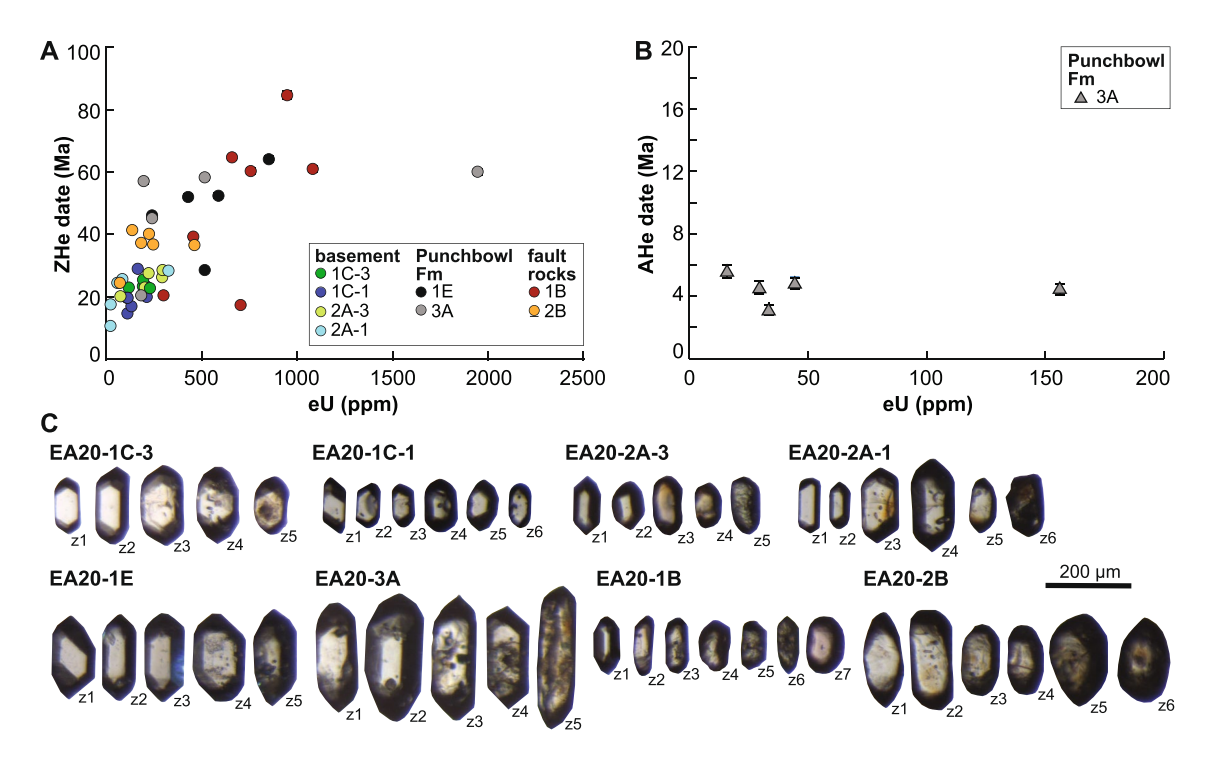


Figure 3. (a) Individual ZHe date as a function of eU, classified by sample. eU concentration calculated based on grain dimensional mass. (b) Apatite (U-Th)/He (AHe) date as a function of eU for Punchbowl Formation (Fm) sample 3A. eU concentration calculated from Ca-based mass (Guenthner et al., 2016). Error bars in A and B are 2σ analytical uncertainty (hidden behind ZHe data points). (c) Plane-polarized light stereoscopic images of zircon grains analyzed in this study.

present in Punchbowl Fm sample 3A. Zircon grains were selected following the approach of Ault et al. (2018) to encapsulate the range of visual metamictization in each sample.

Zircon and apatite grains were imaged and measured using a stereoscope and Leica software, and loaded into 1 mm Nb tubes in the M<sup>2</sup>SL. All grains were analyzed for U, Th, and He, and Sm and Ca was also measured for apatite at the Arizona Radiogenic Helium Dating Lab (ARHDL) at the University of Arizona following standard apatite and zircon degassing, spiking, and dissolution protocols (Reiners, 2005). Apatite fragments from samples 1C-2, 1B, 1D, 1E, 2A-3, 2A-2, and 2A-1 were analyzed for AFT thermochronometry at the Arizona FT Lab. ZHe, AHe, and AFT analytical details are provided in the Supporting Information S1.

# 4. Thermochronometry Results

We acquired 45 individual zircon ZHe dates from eight samples (Figures 2 and 3, and S1 in Supporting Information S1; Table 1), six individual AHe dates from one sample (Figure 3; Table S2 in Supporting Information S1), and AFT dates from eight samples (Tables S3 and S4 in Supporting Information S1). For ZHe and AHe results, we report the unweighted sample mean and  $1\sigma$  standard deviation of the mean for samples with <20% standard deviation. For sample dates >20% standard deviation of the mean, we report the range of individual dates with  $2\sigma$  analytical error (Flowers & Kelley, 2011). We report AFT dates as the central date  $\pm 1\sigma$  standard deviation (Galbraith, 1990). Across the whole dataset, zircon grains selected for ZHe analysis range from faceted, clear grains to honey to light brown, translucent grains with rounded tips (Figure 3c). It is difficult to evaluate the relationship between visual metamictization and eU concentration in our samples because there is limited intra- and inter-sample eU variability and, with a few exceptions, most grains exhibit low visual metamictization (Figure 3c).

Mean ZHe dates from basement samples are  $23.7 \pm 1.1$  Ma (1C-3, n = 5) with 136-239 ppm eU and  $25.1 \pm 3.5$  Ma (2A-3, n = 5) with 97-316 ppm eU (Figures 2c, 2d and 3a). Samples 1C-1 and 2A-1 have individual ZHe dates of  $14.7 \pm 0.5$  Ma- $29.0 \pm 0.8$  Ma (1C-1, n = 6) over 119-212 ppm eU, and  $10.7 \pm 0.3$  Ma- $28.4 \pm 0.8$  Ma (2A-1, n = 6) over 97-386 ppm eU, respectively (Figures 2c, 2d and 3a). The Th/U ratio ranges for all basement samples are the highest of the data set, ranging from 0.41 to 0.66, with two outliers of 0.29 in sample 1C-3 and 0.74 in sample

ARMSTRONG ET AL. 7 of 20



 Table 1

 Zircon (U-Th)/He Thermochronometry Data From Sites EA20-1 and EA20-2, as Well as Sample EA20-3A Along the Punchbowl Fault, CA

Sample	Mass <sup>a</sup> (μg)	Rs <sup>b</sup> (µm)	r <sup>c</sup> (μm)	l <sup>d</sup> (μm)	U (ng)	±1σ (ng)	Th (ng)	±1σ (ng)	eU <sup>e</sup> (ppm)	<sup>4</sup> He (pmol)	$\pm 1\sigma$ (pmol)	Ft <sup>f</sup>	Raw Date (Ma)	Error <sup>g</sup> (Ma)	Corr. Date (Ma)	Error <sup>a</sup> (Ma)
EA20-10	C-3, crysta	alline bas	sement													
z1	1.5	33.5	27	135	0.302	0.004	0.190	0.003	254	0.028	0.000	0.70	14.8	0.2	22.9	0.3
z2	3.6	48.9	40	180	0.716	0.010	0.435	0.006	207	0.078	0.001	0.78	17.6	0.2	23.5	0.3
z3	4.7	53.3	45	187	0.931	0.013	0.263	0.004	191	0.097	0.001	0.80	18.0	0.3	23.4	0.3
z4	4.6	55.4	48	181	0.899	0.013	0.375	0.005	192	0.106	0.001	0.80	19.8	0.3	25.5	0.4
z5	2.3	44.5	38	136	0.284	0.004	0.136	0.002	117	0.028	0.000	0.77	16.7	0.2	23.0	0.3
EA20-10	C-1, crysta	ılline bas	sement													
z1	1.1	32.5	27	122	0.219	0.003	0.105	0.002	211	0.017	0.000	0.69	12.8	0.2	20.0	0.3
z2	0.8	30.4	26	109	0.099	0.001	0.039	0.001	110	0.005	0.000	0.69	9.0	0.1	14.7	0.2
z3	0.9	31.9	27	104	0.097	0.001	0.052	0.001	108	0.007	0.000	0.69	12.5	0.2	19.7	0.3
z4	1.9	42.6	37	124	0.270	0.004	0.140	0.002	131	0.020	0.000	0.76	12.1	0.2	17.0	0.2
z5	1.5	42.3	38	123	0.219	0.003	0.109	0.002	111	0.019	0.000	0.76	14.1	0.2	19.7	0.3
z6	0.7	27.8	23	104	0.105	0.002	0.076	0.001	164	0.011	0.000	0.66	16.9	0.2	29.0	0.4
EA20-2	A-3, crysta	alline bas	sement													
z1	1.5	40.1	34	138	0.131	0.002	0.080	0.001	73.2	0.011	0.000	0.74	14.1	0.2	20.2	0.3
z2	1.3	39.8	36	114	0.321	0.005	0.185	0.003	201	0.032	0.000	0.74	16.0	0.2	23.0	0.3
z3	2.5	44.0	37	143	0.713	0.010	0.331	0.005	292	0.081	0.000	0.76	19.0	0.3	26.3	0.4
z4	1.3	37.8	172	108	0.308	0.004	0.143	0.002	294	0.036	0.000	0.74	19.5	0.3	28.6	0.4
z5	1.5	38.5	32	136	0.381	0.006	0.183	0.003	221	0.043	0.000	0.73	19.0	0.3	27.6	0.4
EA20-2	A-1, crysta	alline bas	sement													
z1	1.2	53.8	44	221	0.099	0.001	0.063	0.001	21.0	0.005	0.000	0.79	8.3	0.1	10.7	0.2
z2	0.8	61.9	49	236	0.172	0.003	0.078	0.001	21.9	0.014	0.000	0.82	14.1	0.2	17.6	0.2
z3	3.7	48.7	41	170	0.791	0.011	0.337	0.005	228	0.080	0.000	0.78	17.1	0.2	22.8	0.3
z4	6.0	48.9	42	162	1.038	0.015	0.445	0.006	325	0.131	0.001	0.78	21.3	0.3	28.4	0.4
z5	1.5	77.7	69	218	0.515	0.007	0.237	0.003	57.1	0.063	0.000	0.85	20.5	0.3	24.5	0.3
z6	2.5	66.9	59	198	0.478	0.007	0.293	0.004	83.3	0.062	0.000	0.83	20.9	0.3	25.7	0.3
EA20-11	E, Punchb	owl Fm.														
z1	4.4	54.7	47	196	2.151	0.031	0.248	0.004	428	0.482	0.003	0.80	40.4	0.6	52.0	0.8
z2	4.4	52.6	43	201	4.024	0.058	0.490	0.007	851	1.104	0.007	0.79	49.3	0.7	64.1	1.0
z3	5.2	55.2	45	209	2.857	0.041	0.399	0.006	515	0.355	0.002	0.80	22.3	0.3	28.6	0.4
z4	6.0	55.7	49	205	3.481	0.050	0.340	0.005	587	0.787	0.005	0.80	40.9	0.6	52.4	0.8
z5	5.5	59.6	49	226	1.606	0.023	0.158	0.002	239	0.325	0.001	0.81	36.6	0.5	46.1	0.7
EA20-3A	A, Punchb	owl Fm.														
z1	0.0	64.2	52	261	4.578	0.067	0.696	0.010	515	1.209	0.003	0.82	47.1	0.7	58.3	0.8
z2	0.0	80.4	67	303	2.722	0.040	1.438	0.020	182	0.286	0.004	0.85	17.3	0.3	20.5	0.4
z3	0.0	67.1	53	294	2.424	0.035	1.226	0.018	239	0.540	0.004	0.83	36.8	0.5	45.2	0.6
z4	0.0	65.6	54	246	17.946	0.262	2.727	0.039	1945	4.906	0.021	0.83	48.8	0.7	60.1	0.9
z5	0.0	66.7	51	342	2.213	0.033	1.432	0.020	195	0.640	0.003	0.82	46.4	0.6	57.1	0.8
EA20-1E	B, PSZ															
z1	1.3	35.6	29	136	0.422	0.006	0.094	0.001	299	0.033	0.000	0.71	13.7	0.2	20.5	0.3
z2	1.2	33.1	27	144	0.840	0.012	0.223	0.003	658	0.202	0.001	0.69	41.8	0.6	64.7	0.9
z3	1.2	34.1	27	132	1.038	0.015	0.102	0.001	756	0.228	0.001	0.70	39.7	0.6	60.3	0.9

ARMSTRONG ET AL. 8 of 20



Table 1 Continued																
Sample	Mass <sup>a</sup> (μg)	Rs <sup>b</sup> (µm)	r <sup>c</sup> (μm)	1 <sup>d</sup> (μm)	U (ng)	±1σ (ng)	Th (ng)	±1σ (ng)	eUe (ppm)	<sup>4</sup> He (pmol)	±1σ (pmol)	Ftf	Raw Date (Ma)	Error <sup>g</sup> (Ma)	Corr. Date (Ma)	Error <sup>g</sup> (Ma)
z4	1.5	41.7	37	122	1.659	0.024	0.200	0.003	1081	0.402	0.002	0.76	43.5	0.6	61.0	0.9
z5	1.3	37.5	32	116	1.099	0.016	0.168	0.002	703	0.073	0.000	0.73	11.9	0.2	17.4	0.3
z6	1.0	32.4	26	757	0.525	0.008	0.195	0.003	455	0.077	0.000	0.73	25.1	0.4	39.3	0.6
<b>z</b> 7	2.5	46.1	41	134	1.954	0.028	0.243	0.004	947	0.682	0.004	0.78	62.5	0.9	84.6	1.2
EA20-2H	EA20-2B, fault core gouge (undifferentiated)															
z1	4.7	53.8	44	121	1.164	0.017	0.174	0.003	223	0.202	0.001	0.73	31.1	0.4	40.2	0.5
z2	7.5	61.9	49	236	1.097	0.016	0.309	0.005	135	0.210	0.001	0.82	33.2	0.4	41.4	0.6
z3	3.1	48.7	41	170	0.649	0.009	0.199	0.003	182	0.105	0.000	0.77	28.0	0.4	37.3	0.5
z4	3.1	49.3	42	162	1.241	0.018	0.223	0.003	461	0.193	0.000	0.78	27.6	0.4	36.6	0.5
z5	7.4	77.3	69	218	0.878	0.013	0.274	0.004	70.3	0.104	0.000	0.85	20.5	0.3	24.5	0.3
z6	6.3	66.7	59	198	2.014	0.029	0.532	0.008	245	0.346	0.001	0.83	29.9	0.4	36.8	0.5

<sup>a</sup>Dimensional mass calculated from grain measurements. <sup>b</sup>Equivalent spherical radius. <sup>c</sup>r = grain half-width. <sup>d</sup>l = grain length. <sup>e</sup>eU calculated as [U] + 0.235 \*[Th], Shuster et al. (2006). <sup>f</sup>Ft = alpha ejection correction of Hourigan et al. (2005). <sup>g</sup>Error = 1σ analytical uncertainty propagated from the U, Th, He contents and grain length measurements.

1C-1 (Figures 2e and 2f). Punchbowl Fm samples yield individual ZHe dates of  $28.6 \pm 0.9$  Ma- $64.1 \pm 1.9$  Ma (1E, n = 5) and  $20.5 \pm 0.4$  Ma- $60.1 \pm 0.9$  Ma (3A, n = 5; Figures 2c and 3a). These samples have broader eU ranges of 298-948 ppm and 182-1,945 ppm, respectively (Figure 3a). Zircon grains in Punchbowl Fm sample 1E have Th/U ratios of 0.10-0.14 and sample 3A yields a Th/U ratios of 0.16-0.66 (Figure 2e).

Individual ZHe dates from PSZ sample 1B range from  $17.4 \pm 0.5$  Ma to  $84.6 \pm 2.5$  Ma (n = 7), with eU concentrations ranging from 345 to 1,102 ppm. Fault gouge sample 2B yields a mean date of  $36.1 \pm 6.0$  Ma (n = 6), with a narrow eU range of 128–417 ppm (Figures 2c, 2d and 3a). The Th/U ratios for fault gouge samples 1B and 2B are 0.10–0.38 and 0.15–0.32, respectively (Figures 2e and 2f). Across all samples, there are no obvious intrasample trends between ZHe dates and equivalent spherical radius (Rs), a proxy for zircon grain size and another potential source of date variation data (Figure S1a in Supporting Information S1).

AHe and AFT analyses from a subset of samples provide a comparison to ZHe results. Individual AHe dates from the Punchbowl Fm sample 3A are  $3.0 \pm 0.8$  Ma- $5.5 \pm 0.8$  Ma (n = 5) with 17–157 ppm eU (Table S2 in Supporting Information S1). There is no trend between AHe date and Rs (Figure S1b in Supporting Information S1). Most samples analyzed for AFT thermochronometry are plagued by low apatite yield and grains with minimal tracks, resulting in large individual grain-level and sample-level uncertainties. Nevertheless, our AFT data can still inform general thermal histories by exploiting intra- and inter-sample data pattern scatter. We report seven AFT central dates (Tables S3 and S4 in Supporting Information S1). The central date for sample 1C-2 is  $18.1 \pm 13.2$  Ma (n = 4), 2A-3 is  $8.7 \pm 8.8$  Ma (n = 4), 2A-2 is  $10.1 \pm 4.2$  Ma (n = 10), 2A-1 is  $16.5 \pm 17.0$  Ma (n = 2), 1E is  $12.2 \pm 1.5$  Ma (n = 18), 1B is  $18.4 \pm 7.2$  Ma (n = 3), and 1D is  $9.0 \pm 9.1$  Ma (n = 5); Tables S3 and S4 in Supporting Information S1).

# 5. Zircon (U-Th)/He Data Patterns and Preliminary Interpretations

Zircon (U-Th)/He data from all samples define a positive date-eU trend from  $\sim 10$  to 60 Ma and  $\sim 20-700$  ppm eU with a plateau at  $\sim 65$  Ma at > 700 ppm eU (Figure 3a). Importantly, data from the PSZ and gouge are part of the overall ZHe date-eU pattern (Figures 2 and 3a). Prior work indicates that exhumed PF rocks experienced peak burial conditions of  $\sim 110^{\circ}$ C (Polissar et al., 2011). At these ambient temperatures, the kinetics of the ZHe system should be sensitive to friction-generated heat from earthquakes that ruptured through present-day exposures as indicated by biomarker results (Savage & Polissar, 2019). If these events occurred between  $\sim 4$  and 1 Ma (Coffey, Savage, et al., 2019; Schulz & Evans, 1998, 2000), then the antiquity of the ZHe dates from the PSZ and gouge (> 4 Ma) and the ZHe date-eU pattern defined by all grains regardless of position within or outside the PF

ARMSTRONG ET AL. 9 of 20



indicates that the PSZ and gouge grains did not experience *complete* (i.e., >90%) He loss at that time or we would expect all grains to have dates <4 Ma regardless of eU. We note that there is some second order scatter around this overall ZHe date-eU trend that may reflect U and Th zonation, a variable we cannot constrain because the grains were consumed during (U-Th)/He analysis (Guenthner et al., 2013). ZHe data from the Punchbowl Fm are from detrital grains, and inherited He and radiation damage (cf. Guenthner et al., 2015) may contribute to this dispersion. Interestingly, one PSZ analysis (~17 Ma, 703 ppm eU) appreciably deviates from our observed date-eU trend. This may be explained by partial He loss during coseismic temperature rise, which we will explore further.

The ZHe date-eU pattern also indicates that PSZ and gouge zircon grains share elements of a common thermal history with material outside the PF. Although basement zircon crystals yield a restricted range of low eU values (<400 ppm), their ZHe dates are similar to Punchbowl Fm ZHe dates over the same eU values (Figure 3a). This implies some Punchbowl Fm grains could be sourced from the adjacent basement or more distal units of similar age and chemistry. Across all samples, most zircon grains have generally low (<500 ppm) to moderate (500–1,200 ppm) eU values, and low visual metamictization (Figure 3c; cf. Ault et al., 2018). These observations strongly suggest that grains have low accumulated radiation damage, but Raman spectroscopy is required to confirm this (Ginster et al., 2019; Nasdala et al., 2004). The positive ZHe date-eU pattern is characteristic of grains with low accumulated damage (Guenthner et al., 2013). Basement and Punchbowl Fm zircon grains, and PSZ and gouge grains sourced from these units, are likely Phanerozoic in age. If grains were Proterozoic or Archean, we might anticipate an inverse ZHe date-eU relationship across moderate eU values, owing to the old age of the grains and/or long duration(s) at temperatures low enough for damage to accumulate (Ault et al., 2018; Guenthner et al., 2013). We do not know the crystallization age of the basement and more work is required to inform this, however prior detrital zircon U-Pb geochronology of Punchbowl Fm grains indicates the presence and dominance of Phanerozoic zircon (Coffey, Savage, et al., 2019; Hoyt et al., 2018; Ingersoll et al., 2013).

AHe and AFT thermochronometry data provide important constraints on the thermal history of the PF and Punchbowl Fm. AHe dates from Punchbowl Fm sample 3A are uniform at  $\sim$ 4 Ma over  $\sim$ 180 ppm spread in eU, indicating rapid cooling of the Punchbowl Fm adjacent to the PF at that time (Figure 3b). Assuming this phase of exhumation is related to fault slip and transpression on the PF, these dates may represent the best timing constraint of broader PF activity. Robust interpretation of AFT results is hindered by low apatite and track yields (Tables S3 and S4 in Supporting Information S1). However, AFT dates show intrasample scatter and sample central dates do not pass the  $X^2$  test, suggesting different AFT date populations likely reflecting partial resetting over their long-term thermal history. The lack of complete track annealing in sample 1E, characterized by the highest grain yield, indicates the Punchbowl Fm did not experience ambient temperatures >110°C since  $\sim$ 12 Ma, which is consistent with biomarker-derived estimates of burial temperatures of the Punchbowl basin and prior AFT dates from basement rocks implying partial resetting (Blythe et al., 2000; Polissar et al., 2011). Assuming a geothermal gradient of  $\sim$ 30°C/km and surface temperature of 20°C, this indicates our Punchbowl Fm sample was buried  $\sim$ 3 km since the basin developed.

Zircon Th/U values are useful for identifying the source of material in the PSZ and gouge (Figures 2c and 2d; Table 1). Punchbowl Fm samples (1E, 3A) yield Th/U values of 0.10–0.16 and >0.52, with a notable gap in between these Th/U ranges. Basement samples (1C-1, 1C-3, 2A-1, 2A-3) have Th/U > 0.29. At site EA20-1, the Th/U ratios of four grains from PSZ sample 1B overlap with values from Punchbowl Fm sample 1E. The other three grains from sample 1B have Th/U values that overlap with those of basement samples. These relationships require that the PSZ comprises material from both the Punchbowl Fm and the basement. Interestingly, at site EA20-2, the Th/U of gouge grains (2B) do not overlap with those of adjacent basement samples (2A-3, 2A-1). If grains within gouge are derived solely from immediately-adjacent wall rock, then the Punchbowl Fm is the source of material at site EA20-2. This is consistent with the greater fracture intensity and erodibility of the Punchbowl Fm (Dor et al., 2006) and biomarker evidence for mixing of the Punchbowl Fm into the basement-side black ultracataclasite (Savage & Polissar, 2019). Alternatively, these PF Th/U values reflect that the grains are not sourced from the immediate wall rock, requiring >m-scale lateral translation of material along the PF during fault slip.

# 6. Characterization of the Background Thermal History

# 6.1. Modeling Approach and Setup

In order to determine coseismic temperatures along the PF with our ZHe data and to compare our results with previously published biomarker data, we first constrain the background time-temperature (tT) history by leveraging

ARMSTRONG ET AL. 10 of 20

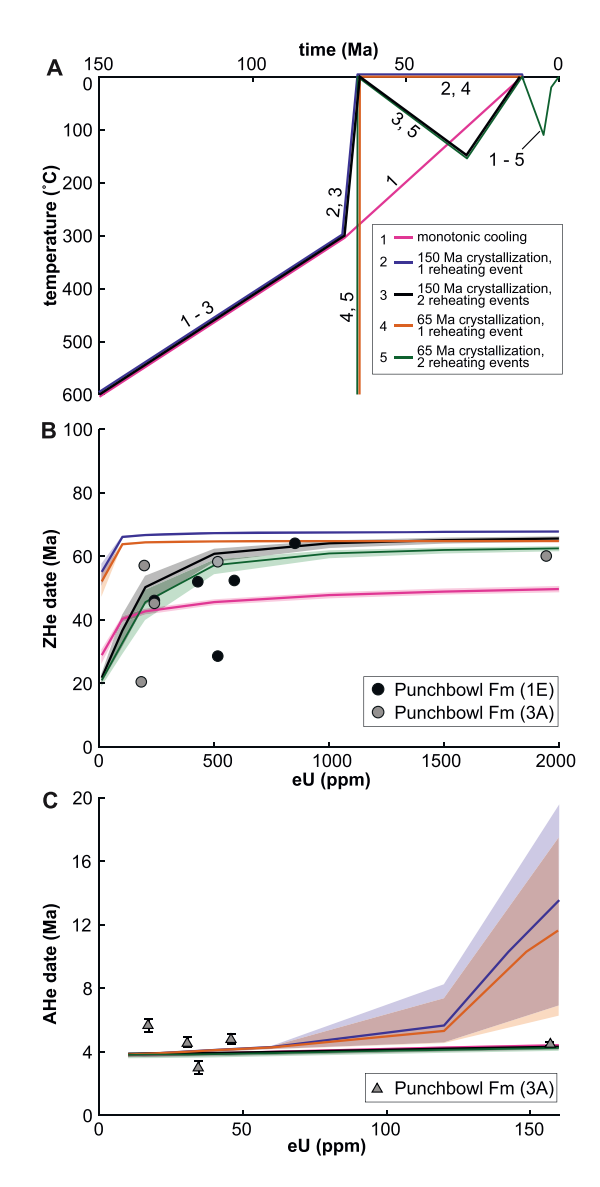


**Figure 4.** (a) End-member time-temperature (tT) paths for the Punchbowl Fm. (b) Predicted ZHe date-eU curves for Punchbowl Fm grains with colors corresponding to tT paths in (a) and observed ZHe date-eU patterns for the Punchbowl Fm (samples 1E, 3A). (c) Predicted AHe date-eU curves and observed AHe date-eU patterns for Punchbowl Fm sample 3A. Models use mean equivalent spherical radius (Rs) for sample 1E and 3A zircon and 3A apatite, and curve envelopes are  $2\sigma$  standard deviation of Rs for zircon and apatite, respectively.

our ZHe and AHe date-eU patterns. To accomplish this, we use only the Punchbowl Fm outside the PF core and not the crystalline basement because more independent geologic and chronologic information exists for the Punchbowl Fm that can inform tT models, including potential zircon crystallization ages and detailed constraints on the thermal history since ~12 Ma. In addition, the Punchbowl Fm samples also have a broader zircon eU range than basement samples, allowing us to better utilize the observed ZHe date-eU trend, and thus damage-He diffusivity relationship, in our modeling.

We employ the forward modeling capabilities of HeFTy (Ketcham, 2005) and He diffusion kinetics from the most recent zircon and apatite radiation damage accumulation and annealing models (ZRDAAM and RDAAM, respectively; Flowers et al., 2009; Guenthner et al., 2013) implemented in HeFTy. We note model outcomes are not likely to differ if the Ginster et al. (2019) annealing kinetics, which are not yet implemented in HeFTy, are applied for the types of tT histories investigated here (Guenthner, 2021). We pose candidate tT paths to generate ZHe and AHe dates over a range of eU comparable to the observed values. Models apply the mean ( $\pm 2\sigma$ ) grain size or equivalent spherical radius (Rs) for the Punchbowl Fm zircon (62  $\pm$  16  $\mu$ m) and apatite (42  $\pm$  10  $\mu$ m).

We consider end-member tT scenarios based on available geologic constraints and inferences from our observed date-eU patterns. Figure 4a illustrates our five candidate tT paths. Paths begin at either 150 Ma (paths 2, 3) or 65 Ma (paths 1, 4, 5), owing to the likely range of crystallization ages of our zircon grains from observed minimal visual metamictization and peaks in detrital zircon U-Pb age data (Hoyt et al., 2018; Ingersoll et al., 2013). The ZHe date plateau at  $\sim$ 60–65 Ma over a broad range of eU values suggests grains cooled rapidly, and thus, paths 2–5 cool rapidly to near-surface temperatures at  $\sim$ 65 Ma. We also explore a scenario in which the zircon grains cool monotonically from  $\sim$ 600°C to 0°C at 12 Ma (path 1).

To evaluate the role of reheating events in development of the observed positive ZHe date-eU pattern, paths 3 and 5 include a reheating event prior to 12 Ma and paths 2 and 4 do not. For simplicity, paths 3 and 5 are characterized by reheating to 150°C symmetric around ~35 Ma. All paths share a common tT history after 12 Ma. They are at the surface (0°C) at 12 Ma, reflecting the unconformity between the San Francisquito and Punchbowl Formations and deposition of the Punchbowl Fm at ~12.5–8.5 Ma (Liu, 1990). Temperatures peak at 110°C at 5 Ma, representing Punchbowl basin burial, consistent with our partially reset AFT data and prior biomarker work (Polissar et al., 2011). Finally, all paths cool after 5 Ma, reflecting exhumation during the time the PF is thought to be active. Details of our forward model setup, including model inputs and tT constraints, are reported in Table S5 in Supporting Information S1 following the reporting protocol of Flowers et al. (2015).

# **6.2.** Model Outcomes and Implications

Model-generated ZHe and AHe date-eU curves from each prescribed tT path are compared with Punchbowl Fm ZHe data and AHe data (Figure 4). Paths with two reheating events best predict the observed ZHe and AHe date-eU patterns. Specifically, tT histories with two reheating events (paths 3, 5) reproduce the observed steep positive ZHe date-eU trend at <700 ppm eU, the ZHe date plateau at <60–65 Ma at >700 ppm eU, and uniform <4 Ma AHe dates regardless of eU (Figures 4b and 4c). In contrast, paths 2 and 4, which remain at surface temperatures between 65 and 12 Ma, predict <65 Ma ZHe dates at >100 ppm eU, which are older than what is observed. These paths also predict markedly older AHe dates at high eU than the observed AHe results. Monotonic cooling since <150 Ma (path 1) yields a ZHe date-eU plateau that is too young relative to observed data. In

ARMSTRONG ET AL. 11 of 20

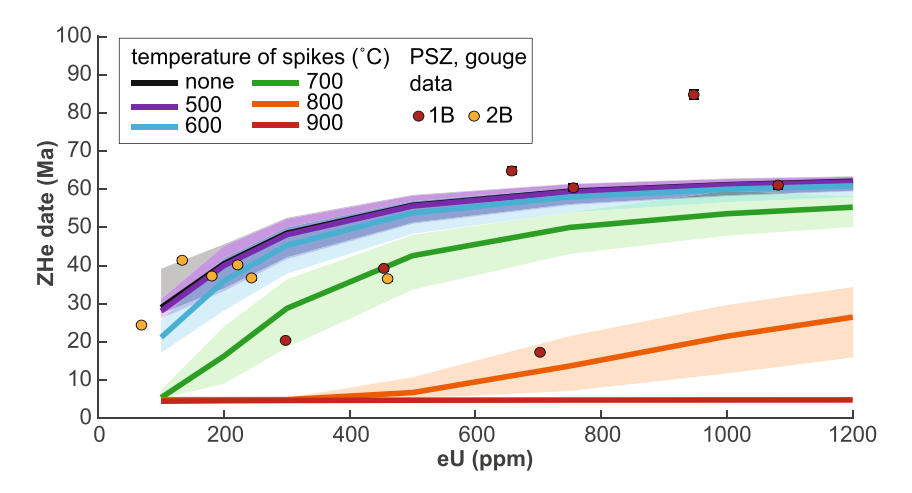


Figure 5. Predicted ZHe date-eU curves for principal slip zone (PSZ) and gouge grains with hypothetical temperature "spikes" simulating coseismic friction-generated heat events superimposed on the representative background tT path (path 3 in Figure 4) in HeFTy. 100 earthquake events are represented as  $\sim$ 30 s temperature spikes that are 1,000 years apart beginning at 5 Ma. The temperature spikes in each model are 500°C, 600°C, 700°C, 800°C, or 900°C (red, orange, green, blue, purple, respectively). The predicted ZHe date-eU curve with no earthquake temperature rise (black) is shown for reference. Observed ZHe date-eU patterns for the PSZ and gouge (samples 1 and 2B, respectively) are shown. Models use mean equivalent spherical radius (Rs) for sample 1 and 2B zircon and curve envelopes are  $2\sigma$  standard deviation of Rs.

addition, it is geologically unlikely that detrital Punchbowl Fm grains were not exposed at the surface since the time of crystallization. In summary, models indicate detrital grains comprising the Punchbowl Fm experienced an initial Eocene-Oligocene reheating event prior to deposition of the Punchbowl Fm and subsequent reheating during Punchbowl basin development. The exact timing, duration, and geologic significance of the initial Eocene-Oligocene heating event is not known. The transition from burial during Punchbowl basin development to exhumation and basin inversion may reflect a change from regional transtension to transpression and oblique slip along the PF.

Thermal history models also support the inference that zircon grains from the Punchbowl Fm are likely Phanerozoic. Reproducing the observed ZHe date-eU pattern is challenging if the grains are Precambrian and experienced prolonged residence at near-surface conditions (Figure S2 in Supporting Information S1). If analyzed grains were Precambrian, then it would require that they resided for a substantial period of geologic time before ~65 Ma at >200–500°C, or temperatures where they would not accumulate radiation damage to be compatible with the lack of visual metamictization (Ault et al., 2018; Ginster et al., 2019; Guenthner et al., 2013). Prior thermochronometry studies indicate most Proterozoic and Archean crystalline basement in the North American Cordillera has been previously exhumed prior to ~65 Ma (Ault et al., 2018; DeLucia et al., 2018; Flowers et al., 2020; Jensen et al., 2018; Johnson et al., 2017; Orme et al., 2016).

# 7. Evaluating Coseismic Temperature Rise With Numerical Models

Thermochronometry data patterns suggest past coseismic temperature rise on the PF was insufficient to *completely* reset ZHe dates from zircon in the PSZ at site EA20-1 and in gouge at site EA20-2. If slip on the PF occurred at the time of our AHe dates and generated coseismic temperatures sufficient to completely reset the ZHe system, then we might expect uniform ~4 Ma ZHe dates regardless of eU from these samples, which we do not observe. Instead, the antiquity of our ZHe dates imply partial to no He loss occurred. Here, we use three different numerical modeling approaches to constrain peak coseismic temperatures and evaluate the effect of partial He loss on ZHe dates.

# 7.1. Background Thermal History With Superimposed Temperature Rise

We first model the effect of hypothetical coseismic friction-generated heat due to repeated earthquakes on ZHe date-eU trends using our background tT path (Figure 5). Because all grains broadly define the same date-eU pattern, we assume that the background tT path for the Punchbowl Fm (path 3; Figure 4) applies to the PSZ and

ARMSTRONG ET AL. 12 of 20

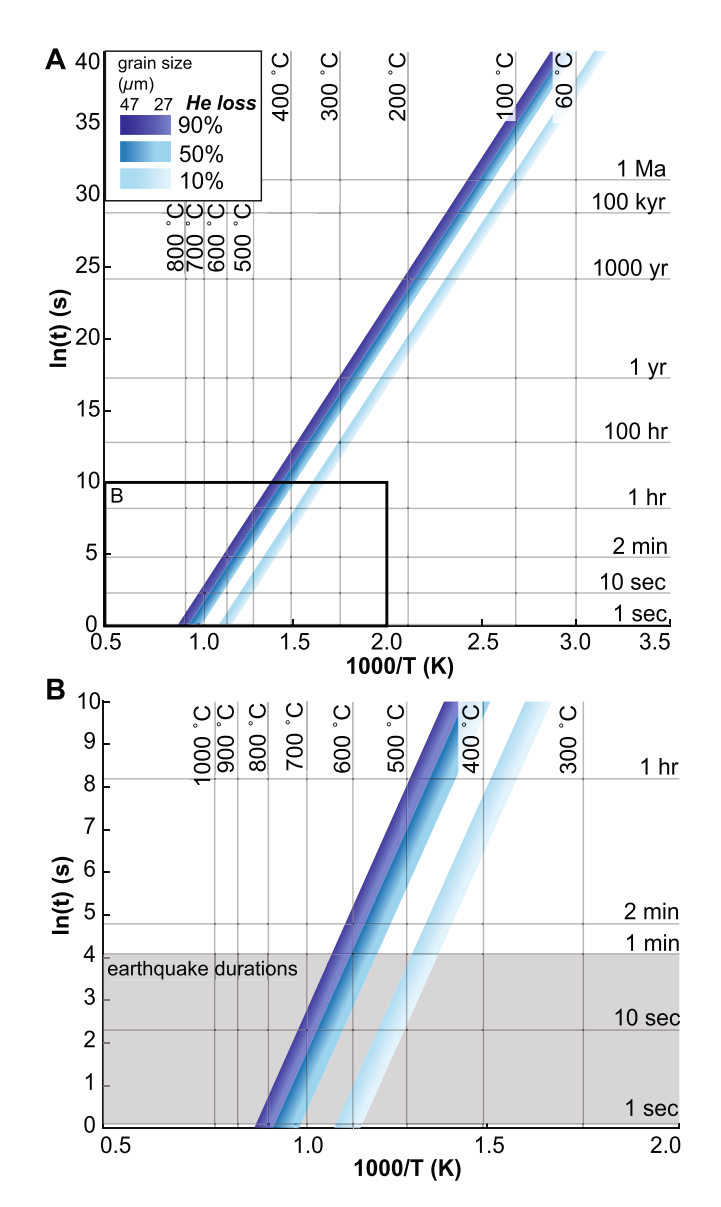


**Figure 6.** (a) Zircon 90%, 50%, and 10% fractional He loss contours as a function of the inverse of temperature (T) and time (t) calculated from a square-pulse heating event. Calculations use activation energy and frequency factor values from grains with low damage from Guenthner et al. (2013) and Rs from 27 to 47  $\mu$ m (light color to dark color, respectively; encompassing the range of PSZ and gouge grain mean Rs  $\pm$  2 $\sigma$ ). (b) Enlarged portion of A, highlighting the relationships of fractional loss contours at earthquake timescales (1–60 s, gray shaded region).

gouge data as well. We superimpose temperature spikes on path 3 and use HeFTy to model predicted ZHe dates over a range of eU. Models incorporate 100 earthquake events, which are represented by  $\sim\!\!30$  s temperature spikes to 500, 600, 700, 800, or 900°C, occurring 1,000 years apart, and beginning at 5 Ma. The temperature pulses last  $\sim\!\!30$  s because that is the minimum time interval HeFTy can resolve. The 1000-year recurrence interval allows the model to return to ambient temperature following each temperature spike. Models use a Rs of 37  $\mu$ m ( $\pm 2s$ ) and eU range of 100–1200 ppm. We again apply the ZRDAAM (Guenthner et al., 2013) to allow radiation damage accumulation and annealing and He diffusion to evolve as a function of time and temperature. Details of the model setup are reported in Table S6 in Supporting Information S1.

Models yield variable ZHe date-eU patterns depending on the magnitude of temperature rise (Figure 5). Time-temperature paths with 500-800°C temperature spikes predict positive ZHe date-eU trends, but with younger dates at progressively higher eU values with increasing peak temperature. Temperature spike models result in progressively higher fractional He loss for any given eU value as the peak coseismic temperature increases. For example, the 900°C model predicts uniform ~5 Ma dates regardless of eU because this temperature is sufficient to induce complete He loss from grains at that time. For comparison, we also model a single earthquake with peak temperatures of 500-900°C (Figure S3 in Supporting Information S1). These results illustrate there is negligible He loss when the peak temperature is 800°C or less and modest He loss at peak temperatures ~900°C. Most PSZ and gouge ZHe dates overlap with the 500 and 600°C predicted ZHe date-eU trends for models with 100 events. However, two PSZ dates and one gouge date overlap with the 700°C model and one PSZ date overlaps the 800°C curve. Although we cannot rule out the effects of U and Th zonation, or inherited He damage or inherited He in the case of detrital grains, on our ZHe dates, these comparisons suggest different grains experienced partial He loss associated with spatially variable coseismic temperatures. We note that the temperatures required to induce similar magnitudes of He loss would be higher for shorter heating intervals.

### 7.2. Fractional He Loss in Variably Damaged Zircon

The prior modeling exercise assumes that we have adequately characterized the background thermal history and is limited by the durations of peak temperatures that HeFTy can resolve. We therefore consider two additional approaches to bracket coseismic temperatures with our data. We first constrain the peak coseismic temperatures by quantifying He diffusion in zircon for different magnitudes and durations of temperature rise. Figure 6 is a "pseudo-Arrhenius" diagram with contours of zircon fractional (90%, 50%, 10%) He loss for a spherical diffusion domain calculated as a function of time, temperature, and grain radius for a square-pulse heating event,

where the magnitude and duration of heating are inversely related (Reiners, 2009). We construct 90% and 10% fractional He loss contours because these percentages are conventionally defined as the upper and lower bounds of the He partial retention zone (Dodson, 1973) and the 90% contour approximates complete He loss. We use experimentally-derived diffusion kinetic parameters (activation energy,  $E_a$ , and frequency factor,  $D_0$ ) for low accumulated radiation damage (analogous to Mudtank diffusion kinetics, Table S7 in Supporting Information S1; Guenthner et al., 2013), because our grains have dominantly low eU values, are likely Phanerozoic age, and have limited metamictization. We apply an Rs of 27–47  $\mu$ m, or the mean grain size  $\pm 2\sigma$  for PSZ and gouge grains. For comparison, Figure S4 in Supporting Information S1 illustrates the pseudo-Arrhenius relationships for zircon grains encapsulating a range of accumulated radiation damage from no damage (Reiners et al., 2004) to medium,

ARMSTRONG ET AL. 13 of 20



high, and very high (amorphous) damage (Table S7 in Supporting Information S1; Guenthner et al., 2013). He diffusion kinetic parameters are derived from diffusion experiments conducted using prograde-retrograde heating schedules with 10–15 intervals of heating for 90-min to 150 to 500°C (Guenthner et al., 2013; Reiners et al., 2004).

We consider the temperatures required to induce He loss at earthquake timescale durations (1–60 s), consistent with heating durations inferred in Savage and Polissar (2019). Because most PSZ and gouge grains define the same ZHe date-eU trend as grains from outside the PF, calculated temperatures provide an upper bound on coseismic temperature rise. Temperatures required to induce 90% He loss are  $\sim$ 790–850°C for 1 s,  $\sim$ 670–740°C for 10 s, and  $\sim$ 600–660°C for 60 s. If grains experienced partial He loss, then temperatures are lower (Figure 6b). For example, 50% He loss requires temperatures of  $\sim$ 750–810°C for 1 s,  $\sim$ 650–700°C for 10 s, and  $\sim$ 570–640°C for 60 s. If grains are characterized by moderate damage (purple line in Figure S4 in Supporting Information S1; analogous to B231 of Guenthner et al., 2013) then they would require temperatures >1,100°C to induce appreciable He loss (Figure S4 in Supporting Information S1). Complete He loss at temperatures <600°C requires effectively amorphous grains (i.e., black line in Figure S4 in Supporting Information S1; very high damage analogous to N17 of Guenthner et al., 2013), which we do not observe in our dated aliquots.

### 7.3. Shear Heating Model

We next explore fault slip conditions that yield temperatures sufficient to induce He loss in low radiation damage zircon grains with a model that calculates peak surface temperature rise during an individual earthquake and corresponding zircon fractional He loss (Text S2 in Supporting Information S1; Fechtig & Kalbitzer, 1966; Lachenbruch, 1986; McDermott et al., 2017). Models consider a range of displacements (D, 0.1–5 m), slip zone half-widths (h, 0.005–5 cm) and coefficients of friction (μ, 0.12–0.6) for a prescribed velocity (V, 1 m/s). Values for model parameters encompass those of Savage and Polissar (2019) and are within the expected range for a large earthquake. Slip zone half-width values reflect observed width of the PSZ (2 cm) at site EA20-1 and the gouge at site EA20-2 (10 cm), as well as smaller half-widths to consider the likelihood that the deforming layer during any given event is narrower than present-day color variations preserved in the fault core architecture. The imposed coefficient of friction spans the measured value for PF gouge material (Kitajima et al., 2010) to values for clay minerals and Byerlee's coefficient of friction (Byerlee, 1978; Moore & Lockner, 2008). Additional details of the model setup are described in Text S2 and Table S8 in Supporting Information S1.

Figure 7 illustrates modeled temperatures along a fault surface (depth, z = 0) as a function of displacement and coefficient of friction (Figure 7a) or slip zone half-width (Figure 7b), together with the temperature-dependent 90%, 50%, and 10% He fractional loss contours. Model results are also shown as % He loss as a function of peak temperature for specific slip zone half-widths (Figure 7c). Analogous to prior work (e.g., Coffey, Ingersoll, & Schmitt, 2019; Lachenbruch, 1986; Savage & Polissar, 2019), modeled temperature rise is sensitive to both slip zone half-width and coefficient of friction. For example, for a given displacement, a thinner deforming zone yields higher temperatures than a wider deforming zone (Figure 7b). Increasing the coefficient of friction from 0.12 to 0.6 (while holding slip zone half-width constant) yields higher peak temperatures (Figure 7a), and we suggest that the coefficient of friction of the PF was likely closer to 0.12 (Kitajima et al., 2010) during PF activity.

This model reveals that >90% He loss is achieved when generated temperatures are >725°C for most parameter combinations relevant for the PSZ at site EA20-1 (Figure 7). For the PSZ, if  $\mu$  and V are constant, then the peak temperatures associated with 90% He loss range from ~725 to 1,050°C for a slip zone half-width of 1 cm down to 0.005 cm (Figure 7c). If the observed thickness of the PSZ approximates the width of the deforming layer, then the generated temperatures induce >90% He loss only at the maximum displacement shown (i.e., 5 m). The thickness of the gouge at site EA20-2 approximates an even broader deforming zone (5 cm half-width), and modeled temperatures (~250°C) induce <10% He loss. For any slip zone half-width, even lower temperatures are required to induce 50% or 10% loss versus 90% He loss.

Importantly, some ZHe dates deviate from the overall date-eU trend and may reflect partial resetting during coseismic temperature rise. This is exemplified by the PSZ zircon grain with 703 ppm eU and a  $\sim$ 17 Ma ZHe date. If we assume that the corresponding ZHe date for this eU value from the background tT history alone is  $\sim$ 60 Ma (Figures 3a and 4b), then the calculated fractional He loss is 75%–78% if coseismic slip occurred

ARMSTRONG ET AL. 14 of 20

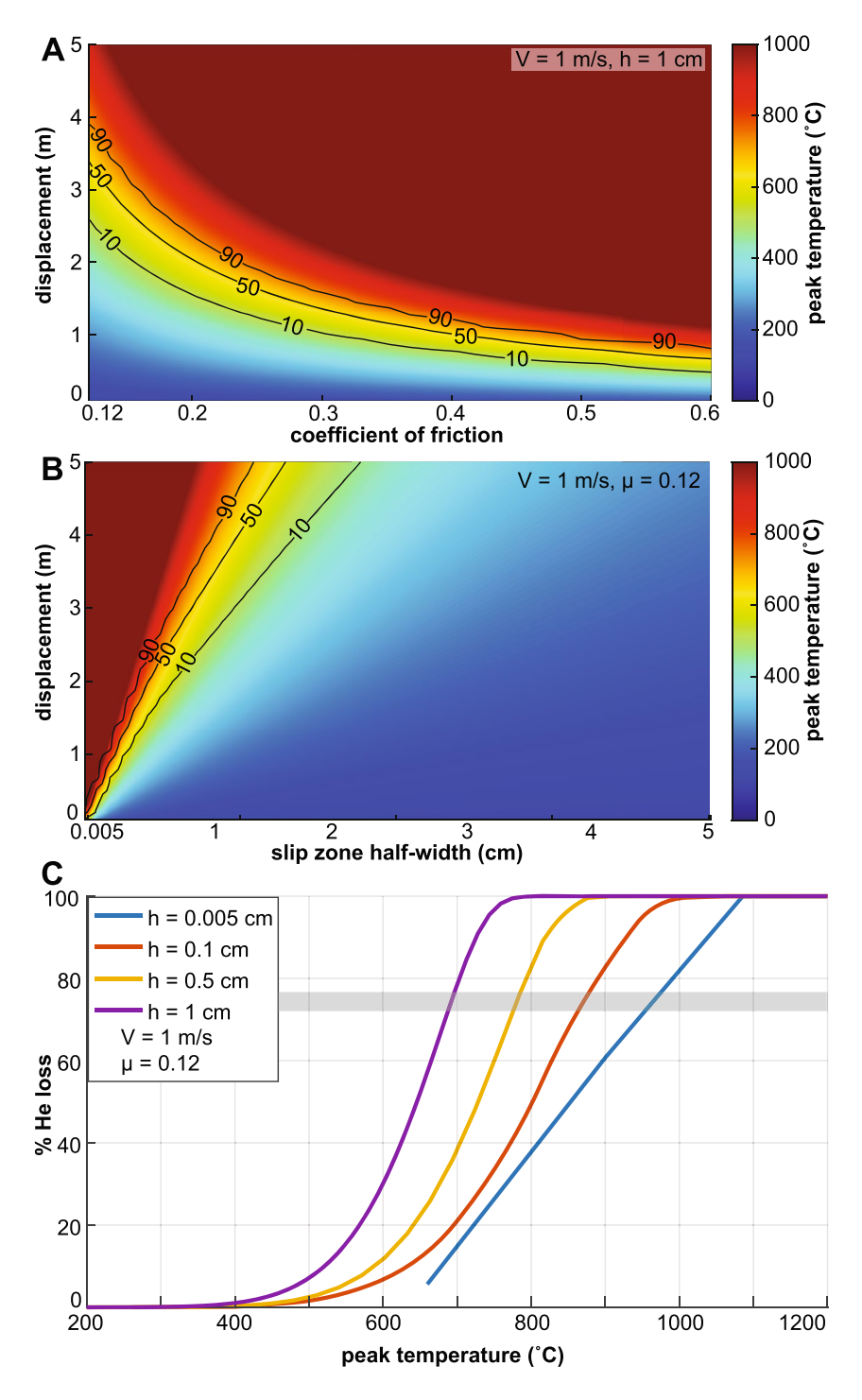


Figure 7. Shear heating model results showing peak temperature rise (color scale at right) at fault surface (depth, z=0) with 10%, 50%, and 90% fractional He loss contours (black lines) calculated from shear heating (Lachenbruch, 1986) and fractional loss (Fechtig & Kalbitzer, 1966) equations. Displacement (y-axis) is 0.01-5 m for each model. (a) Model output varies coefficient of friction ( $\mu$ ) from 0.12 to 0.6 (x-axis) and slip zone half-width (h) is 1 cm (representing observed principal slip zone width of 2 cm at EA20-1). (b) Model output varies h from 0.005 to 5 cm (representing range of h observed in PSZ and gouge) and  $\mu$  is 0.12. (c) % He loss as a function of peak temperature rise for given h values of 0.005 cm (blue), 0.1 cm (red), 0.5 cm (yellow), or 1 cm (purple), where velocity (V) is 1 m/s and  $\mu$  is 0.12. Displacement varies. Gray box shows 75%–78% He loss.

ARMSTRONG ET AL. 15 of 20



between  $\sim$ 4 and 1 Ma. The temperature required to induce 75% He loss is  $\sim$ 680°C for a 1 cm half-width slip zone and  $\sim$ 975°C for a 0.005 cm half-width (Figure 7c).

# 8. Intermethod Comparison and Implications for Punchbowl Fault Evolution

Thermochronometry data patterns and numerical models bracket peak temperatures during earthquake slip along the PF and provide comparison with biomarker analyses. All samples, regardless of lithology and position relative to the PF, yield ZHe dates >10 Ma and broadly define a positive ZHe date-eU trend at low eU values with a plateau in dates at moderate eU values. These data patterns indicate coseismic temperature rise, which likely occurred between ~4 and 1 Ma, did not induce complete He loss in PSZ and gouge grains during that time. Thus, PSZ and gouge ZHe results provide an *upper bound* on coseismic temperature rise and peak temperatures derived from all three models span 600–1,050°C. Although each of the three modeling approaches has different assumptions and parameters, model outcomes overlap in a more restrictive temperature range and bracket peak temperatures to <725–800°C.

Our results reveal general compatibility of estimated coseismic temperatures on the PF derived from ZHe and biomarker data. Comparison between these two methods with different kinetics is best illustrated by (a) evaluating results from the shear heating model applied here and in Savage and Polissar (2019) and (b) considering temperatures inferred from a PSZ ZHe date that may have been partially reset because these values do not solely represent the maxima. Modeled peak temperatures from biomarkers analyses are ~465–620°C for a 1 cm slip zone half-width and ~815–1,065°C for a 0.005 cm half-width (Savage & Polissar, 2019). Temperatures required to induce ~75% He loss to explain the PSZ grain at ~17 Ma that deviates from the ZHe date-eU pattern are ~680–975°C for slip zone half-widths of 1–0.005 cm (Figure 7c). We acknowledge that these ZHe-derived temperatures appear more restrictive because we are considering a single ZHe analysis, and thus constraint on fractional He loss. Nevertheless, temperatures overlap between the two approaches even though thermal maturation of organic matter has a lower activation energy (93 kJ/mol; Savage & Polissar, 2019; Sheppard et al., 2015) than low damage zircon grains (168 kJ/mol; Table S7 in Supporting Information S1; Guenthner et al., 2013), meaning biomarkers may be more easily altered than He is lost from zircon of this damage level for a given thermal history.

ZHe model outcomes, together with observations of variable fault-zone width and presence/absence of a PSZ, imply that the temperature rise can vary over multiple scales. The conditions and mechanics of slip along the PF likely evolved since the fault initiated, yielding variable coseismic temperatures in space and time (cf. Coffey, Savage, et al., 2019). With progressive strain localization and fluid-rock interaction, slip zone half-width and coefficient of friction decrease, but these changes have opposing effects on coseismic temperatures (when holding velocity and displacement constant). Thus, zircon grains may have experienced variable temperatures owing to their evolving position in the deforming layer with time or variable peak temperatures in a given location within a deforming zone. For example, our temperature spike model illustrates that some PSZ and gouge grains are best fit with peak coseismic temperatures of ~700°C and one PSZ grain overlaps with peak temperatures of ~800°C. This complements inferences from Savage and Polissar (2019), who observed different MPI-4 values within and across different sample sites indicative of variations in temperature rise along and across strike from variable slip zone width and localized variations in earthquake properties.

# 9. Conclusions

Developing new geochemical approaches for documenting cryptic coseismic temperature rise and thus past earth-quakes along exhumed faults is important because textural and mineralogical evidence for seismic slip, including the presence of pseudotachylyte, can be overprinted by subsequent deformation and/or fluid-rock interaction. Robustly quantifying this coseismic temperature rise requires intermethod comparison of paleothermometers with different kinetics. Here we leverage prior biomarker evidence for friction-generated heat along the Punchbowl fault and acquire new ZHe and complementary AHe and AFT thermochronometry data from the same sample locations. We infer that analyzed zircon grains are low accumulated radiation damage because of their limited visual metamictization, low to moderate eU, and likely Phanerozoic age. Zircon chemistry reveals that grains entrained within the PSZ and gouge are derived from both the crystalline basement and Punchbowl Fm adjacent to the PF.

ARMSTRONG ET AL. 16 of 20



Acknowledgments

M. Armstrong.

We thank Peter Reiners and Uttam

Chowdhury (UA) for analytical assis-

tance, Robert McDermott (USGS) for

the shear heating model code, and Ryker

Tracy for sample processing. We thank

two anonymous reviewers for thought-

manuscript. Research was supported by a

SCEC award (20153) to A. K. Ault, H. M.

Savage, and P. J. Polissar; NSF CAREER

grant (EAR-165462) to A. K. Ault; and

an NSF Graduate Research Fellowship,

GSA Student Research award, and USU

Geoscience Department scholarships to E.

ful reviews that helped improve the

Zircon (U-Th)/He data patterns suggest friction-generated heat from past seismic slip on the PF was insufficient to *completely* reset ZHe dates in the PSZ and gouge. It is permissible that some PSZ zircon grains may have experienced up to ~75% He loss (or partial resetting) during coseismic temperature rise, but more data is required to evaluate this as well as rule out effects of U and Th zonation on ZHe dates. Thermal history forward models of the Punchbowl Fm bracket the background, long-term thermal history characterized by two burial events, including the development of the Punchbowl basin. Three different numerical modeling approaches, each with different inputs and assumptions, in conjunction with ZHe date-eU patterns, collectively suggest the temperature rise along the PF was <725–800°C for 90% (i.e., near complete) He loss. These peak temperatures are similar to the temperatures recorded by biomarkers, reflecting broad compatibility between the two systems.

# **Data Availability Statement**

All information in the Supporting Information is archived and freely available at figshare.com (https://doi.org/10.6084/m9.figshare.19216953) and ZHe and AHe analyses are available at Geochron.org (http://geochron.org/results.php?pkey=36495).

### References

- Armstrong, P. A., Ehlers, T. A., Chapman, D. S., Farley, K. A., & Kamp, P. J. (2003). Exhumation of the central Wasatch Mountains, Utah: 1. Patterns and timing of exhumation deduced from low-temperature thermochronology data. *Journal of Geophysical Research*, 108(B3), 2172. https://doi.org/10.1029/2001jb001708
- Ault, A. K. (2020). Hematite fault rock thermochronometry and textures inform fault zone processes. *Journal of Structural Geology*, 133, 104002. https://doi.org/10.1016/j.jsg.2020.104002
- Ault, A. K., Guenthner, W. R., Moser, A. C., Miller, G. H., & Refsnider, K. A. (2018). Zircon grain selection reveals (de) coupled metamictization, radiation damage, and He diffusivity. *Chemical Geology*, 490, 1–12. https://doi.org/10.1016/j.chemgeo.2018.04.023
- Ault, A. K., Reiners, P. W., Evans, J. P., & Thomson, S. N. (2015). Linking hematite (U-Th)/He dating with the microtextural record of seismicity in the Wasatch fault damage zone, Utah, USA. *Geology*, 43(9), 771–774. https://doi.org/10.1130/g36897.1
- Barth, A. P. (1990). Mesozoic rock units in the upper plate of the Vincent thrust fault, San Gabriel Mountains, Southern California.
- Barth, A. P., Tosdal, R., Wooden, J., & Howard, K. (1997). Triassic plutonism in southern California: Southward younging of arc initiation along a truncated continental margin. *Tectonics*, 16(2), 290–304. https://doi.org/10.1029/96tc03596
- Blythe, A. E., Burbank, D. W., Farley, K. A., & Fielding, E. J. (2000). Structural and topographic evolution of the central Transverse Ranges, California, from apatite fission-track, (U-Th)/He and digital elevation model analyses. *Basin Research*, 12, 97–114. https://doi.org/10.1046/j.1365-2117.2000.00116.x
- Byerlee, J. (1978). Friction of rocks. In Rock friction and earthquake prediction (pp. 615-626). Springer. https://doi.org/10.1007/978-3-0348-7182-2 4
- Calzolari, G., Ault, A. K., Hirth, G., & McDermott, R. G. (2020). Hematite (U-Th)/He thermochronometry detects asperity flash heating during laboratory earthquakes. *Geology*, 48(5), 514–518. https://doi.org/10.1130/g46965.1
- Chester, F., & Logan, J. (1986). Implications for mechanical properties of brittle faults from observations of the Punchbowl fault zone, California. Pure and Applied Geophysics, 124(1–2), 79–106. https://doi.org/10.1007/bf00875720
- Chester, F., & Logan, J. (1987). Composite planar fabric of gouge from the Punchbowl Fault, California. *Journal of Structural Geology*, 9(5–6), 621–IN626. https://doi.org/10.1016/0191-8141(87)90147-7
- Chester, F. M. (1983). Mechanical properties and fabric of the Punchbowl fault zone, California. Texas A&M University.
- Chester, F. M., & Chester, J. S. (1998). Ultracataclasite structure and friction processes of the Punchbowl fault, San Andreas system, California. Tectonophysics, 295(1–2), 199–221. https://doi.org/10.1016/s0040-1951(98)00121-8
- Chester, F. M., Evans, J. P., & Biegel, R. L. (1993). Internal structure and weakening mechanisms of the San Andreas fault. *Journal of Geophysical Research*, 98(B1), 771–786. https://doi.org/10.1029/92jb01866
- Chester, J. S., Chester, F. M., & Kronenberg, A. K. (2005). Fracture surface energy of the Punchbowl fault, San Andreas system. *Nature*, 437(7055), 133–136. https://doi.org/10.1038/nature03942
- Coffey, G. L., Savage, H. M., Polissar, P. J., Rowe, C. D., & Rabinowitz, H. S. (2019). Hot on the trail: Coseismic heating on a localized structure along the muddy mountain fault, Nevada. *Journal of Structural Geology*, 120, 67–79. https://doi.org/10.1016/j.jsg.2018.12.012
- Coffey, K. T. (2015). Oligocene-Miocene sedimentary and volcanic strata of the Vincent gap region, Eastern San Gabriel Mountains, Southern California, USA, and their tectonic significance. University of California.
- Coffey, K. T., Ingersoll, R. V., & Schmitt, A. K. (2019). Stratigraphy, provenance, and tectonic significance of the punchbowl block, San Gabriel Mountains, California, USA. *Geosphere*, 15(2), 479–501. https://doi.org/10.1130/ges02025.1
- Collettini, C., Viti, C., Tesei, T., & Mollo, S. (2013). Thermal decomposition along natural carbonate faults during earthquakes. *Geology*, 41(8), 927–930. https://doi.org/10.1130/g34421.1
- d'Alessio, M., Blythe, A., & Burgmann, R. (2003). No frictional heat along the San Gabriel fault, California: Evidence from fission-track thermochronology. *Geology*, 31(6), 541–544. https://doi.org/10.1130/0091-7613(2003)031<0541:nfhats>2.0.co;2
- DeLucia, M., Guenthner, W. R., Marshak, S., Thomson, S., & Ault, A. (2018). Thermochronology links denudation of the Great Unconformity surface to the supercontinent cycle and snowball Earth. *Geology*, 46(2), 167–170. https://doi.org/10.1130/g39525.1
- Di Toro, G., Han, R., Hirose, T., De Paola, N., Nielsen, S., & Mizoguchi, K. (2011). Fault lubrication during earthquakes. *Nature*, 471(7339), 494–498. https://doi.org/10.1038/nature09838
- Dodson, M. H. (1973). Closure temperatures in cooling geological and petrological systems. *Contributions to Mineralogy and Petrology*, 40, 259–274. https://doi.org/10.1007/bf00373790

ARMSTRONG ET AL. 17 of 20



- Dor, O., Rockwell, T. K., & Ben-Zion, Y. (2006). Geological observations of damage asymmetry in the structure of the San Jacinto, San Andreas and Punchbowl faults in Southern California: A possible indicator for preferred rupture propagation direction. *Pure and Applied Geophysics*, 163(2), 301–349. https://doi.org/10.1007/s00024-005-0023-9
- Ehlers, T., Willett, S., Armstrong, P., & Chapman, D. (2003). Exhumation of the Central Wasatch Mountains 2: Thermo-kinematics models of exhumation, erosion and low-temperature thermochronometer interpretation. *Journal of Geophysical Research*, 108, 2173. https://doi. org/10.1029/2001jb001723
- Ehlers, T. A., & Farley, K. A. (2003). Apatite (U-Th)/He thermochronometry: Methods and applications to problems in tectonic and surface processes. Earth and Planetary Science Letters, 206(1-2), 1-14. https://doi.org/10.1016/s0012-821x(02)01069-5
- Evans, J. P., Prante, M. R., Janecke, S. U., Ault, A. K., & Newell, D. L. (2014). Hot faults: Iridescent slip surfaces with metallic luster document high-temperature ancient seismicity in the Wasatch fault zone, Utah, USA. *Geology*, 42(7), 623–626. https://doi.org/10.1130/g35617.1
- Fechtig, H., & Kalbitzer, S. (1966). The diffusion of argon in potassium-bearing solids. In *Potassium argon dating* (pp. 68–107). Springer. https://doi.org/10.1007/978-3-642-87895-4\_4
- Flowers, R. M., Farley, K. A., & Ketcham, R. A. (2015). A reporting protocol for thermochronologic modeling illustrated with data from the Grand Canyon. Earth and Planetary Science Letters, 432, 425–435. https://doi.org/10.1016/j.epsl.2015.09.053
- Flowers, R. M., & Kelley, S. A. (2011). Interpreting data dispersion and "inverted" dates in apatite (U-Th)/He and fission-track datasets: An example from the US midcontinent. *Geochimica et Cosmochimica Acta*, 75(18), 5169–5186. https://doi.org/10.1016/j.gca.2011.06.016
- Flowers, R. M., Ketcham, R. A., Shuster, D. L., & Farley, K. A. (2009). Apatite (U-Th)/He thermochronometry using a radiation damage accumulation and annealing model. *Geochimica et Cosmochimica Acta*, 73(8), 2347–2365. https://doi.org/10.1016/j.gca.2009.01.015
- Flowers, R. M., Macdonald, F. A., Siddoway, C. S., & Havranek, R. (2020). Diachronous development of great unconformities before neoproterozoic snowball Earth. *Proceedines of the National Academy of Sciences*, 117(19), 10172–10180. https://doi.org/10.1073/pnas.1913131117
- Galbraith, R. F. (1990). The radial plot: Graphical assessment of spread in ages. International Journal of Radiation Applications and Instrumentation Part D: Nuclear Tracks and Radiation Measurements, 17(3), 207–214. https://doi.org/10.1016/1359-0189(90)90036-w
- Gallagher, K. (1995). Evolving temperature histories from apatite fission-track data. Earth and Planetary Science Letters, 136(3-4), 421-435. https://doi.org/10.1016/0012-821x(95)00197-k
- Gautheron, C., Tassan-Got, L., Barbarand, J., & Pagel, M. (2009). Effect of alpha-damage annealing on apatite (U-Th)/He thermochronology. Chemical Geology, 266, 157–170. https://doi.org/10.1016/j.chemgeo.2009.06.001
- Ginster, U., Reiners, P. W., Nasdala, L., & Chanmuang, C. (2019). Annealing kinetics of radiation damage in zircon. Geochimica et Cosmochimica Acta, 249, 225–246. https://doi.org/10.1016/j.gca.2019.01.033
- Goldsby, D. L., & Tullis, T. E. (2011). Flash heating leads to low frictional strength of crustal rocks at earthquake slip rates. *Science*, 334(6053), 216–218. https://doi.org/10.1126/science.1207902
- Guenthner, W. R. (2021). Implementation of an alpha damage annealing model for zircon (U-Th)/He thermochronology with comparison to a zircon fission track annealing model. *Geochemistry, Geophysics, Geosystems*, 22(2), e2019GC008757. https://doi.org/10.1029/2019gc008757 Guenthner, W. R., Reiners, P. W., & Chowdhury, U. (2016). Isotope dilution analysis of Ca and Zr in apatite and zircon (U-Th)/He chronometry.
- Geochemistry, Geophysics, Geosystems, 17(5), 1623–1640. https://doi.org/10.1002/2016gc006311

  Guenthner, W. R., Reiners, P. W., DeCelles, P. G., & Kendall, J. (2015). Sevier belt exhumation in central Utah constrained from complex zircon
- (U-Th)/He data sets: Radiation damage and He inheritance effects on partially reset detrital zircons. *Bulletin*, 127(3–4), 323–348. https://doi.org/10.1130/b31032.1
- Guenthner, W. R., Reiners, P. W., Ketcham, R. A., Nasdala, L., & Giester, G. (2013). Helium diffusion in natural zircon: Radiation damage, anisotropy, and the interpretation of zircon (U-Th)/He thermochronology. *American Journal of Science*, 313(3), 145–198. https://doi.org/10.2475/03.2013.01
- Holland, H. D., & Gottfried, D. (1955). The effect of nuclear radiation on the structure of zircon. Acta Crystallographica, 8(6), 291–300. https://doi.org/10.1107/s0365110x55000947
- Hoyt, J. F., Coffey, K. T., Ingersoll, R. V., & Jacobson, C. E. (2018). Paleogeographic and paleotectonic setting of the middle Miocene Mint Canyon and Caliente formations, Southern California: An integrated provenance study. (pp. 463–480)Geological Society of America Special. Paper 540
- Ingersoll, R. V., Grove, M., Jacobson, C. E., Kimbrough, D. L., & Hoyt, J. F. (2013). Detrital zircons indicate no drainage link between southern California rivers and the Colorado Plateau from mid-Cretaceous through Pliocene. Geology, 41(3), 311–314. https://doi.org/10.1130/g33807.1
- Jensen, J. L., Siddoway, C. S., Reiners, P. W., Ault, A. K., Thomson, S. N., & Steele-MacInnis, M. (2018). Single-crystal hematite (U-Th)/He dates and fluid inclusions document widespread Cryogenian sand injection in crystalline basement. Earth and Planetary Science Letters, 500, 145–155. https://doi.org/10.1016/j.epsl.2018.08.021
- Johnson, J. E., Flowers, R. M., Baird, G. B., & Mahan, K. H. (2017). Inverted" zircon and apatite (U-Th)/He dates from the front range, Colorado: High-damage zircon as a low-temperature (<50°C) thermochronometer. Earth and Planetary Science Letters, 466, 80–90. https://doi.org/10.1016/j.epsl.2017.03.002</p>
- Kameda, J., Ujiie, K., Yamaguchi, A., & Kimura, G. (2011). Smectite to chlorite conversion by frictional heating along a subduction thrust. Earth and Planetary Science Letters, 305(1–2), 161–170. https://doi.org/10.1016/j.epsl.2011.02.051
- Kanamori, H., & Brodsky, E. E. (2001). The physics of earthquakes. Physics Today, 54(6)34-40. https://doi.org/10.1063/1.1387590
- Ketcham, R. A. (2005). Forward and inverse modeling of low-temperature thermochronometry data. *Reviews in Mineralogy and Geochemistry*, 58(1), 275–314. https://doi.org/10.2138/rmg.2005.58.11
- Ketcham, R. A., Guenthner, W. R., & Reiners, P. W. (2013). Geometric analysis of radiation damage connectivity in zircon, and its implications for helium diffusion. *American Mineralogist*, 98(2–3), 350–360. https://doi.org/10.2138/am.2013.4249
- Kirschner, D. L. (2004). Heat-flow constraints of seismogenic faulting from thermochronology studies of apatites, zircons, and K-feldspars in two exhumed faults of the San Andreas system. Department of Earth and Atmospheric Sciences, Saint Louis University.
- Kitajima, H., Chester, J. S., Chester, F. M., & Shimamoto, T. (2010). High-speed friction of disaggregated ultracataclasite in rotary shear: Characterization of frictional heating, mechanical behavior, and microstructure evolution. *Journal of Geophysical Research*, 115(B8), B08408. https://doi.org/10.1029/2009jb007038
- Kohli, A. H., Goldsby, D. L., Hirth, G., & Tullis, T. (2011). Flash weakening of serpentinite at near-seismic slip rates. *Journal of Geophysical Research*, 116(B3), B03202. https://doi.org/10.1029/2010jb007833
- Lachenbruch, A. H. (1986). Simple models for the estimation and measurement of frictional heating by an earthquake: US Department of the Interior. Geological Survey.
- Lachenbruch, A. H., & McGarr, A. (1990). 10. Stress and heat flow. US Geological Survey Professional Paper (Vol 1515. p. 261).
- Liu, W. (1990) Paleomagnetism of miocene sedimentary rocks in the Transverse ranges: The implications for tectonic history. California Institute of Technology.

ARMSTRONG ET AL. 18 of 20



- Maino, M., Casini, L., Ceriani, A., Decarlis, A., Di Giulio, A., Seno, S., et al. (2015). Dating shallow thrusts with zircon (U-Th)/He thermochronometry—the shear heating connection. *Geology*, 43(6), 495–498. https://doi.org/10.1130/g36492.1
- McDermott, R. G., Ault, A. K., Evans, J. P., & Reiners, P. W. (2017). Thermochronometric and textural evidence for seismicity via asperity flash heating on exhumed hematite fault mirrors, Wasatch fault zone, UT, USA. *Earth and Planetary Science Letters*, 471, 85–93. https://doi.org/10.1016/j.epsl.2017.04.020
- McGarr, A. (1999). On relating apparent stress to the stress causing earthquake fault slip. *Journal of Geophysical Research*, 104(B2), 3003–3011. https://doi.org/10.1029/1998jb900083
- McIntosh, R., Sharp, J., & Wilburn, F. (1990). The thermal decomposition of dolomite. *Thermochimica Acta*, 165(2), 281–296. https://doi.org/10.1016/0040-6031(90)80228-q
- Meisling, K., & Alexander, J. (1993). The San Andreas fault system: Displacement, palinspastic reconstruction, and geologic evolution. A speculative history of the San Andreas fault in the central Transverse Ranges, California, 178, 161.
- Mitchell, S. G., & Reiners, P. W. (2003). Influence of wildfires on apatite and zircon (U-Th)/He ages. Geology, 31, 1025–1028. https://doi.org/10.1130/g19758.1
- Moore, D. E., & Lockner, D. A. (2008). Talc friction in the temperature range 25–400 C: Relevance for fault-zone weakening. Tectonophysics, 449(1–4), 120–132. https://doi.org/10.1016/j.tecto.2007.11.039
- Murakami, M., Yamada, R., & Tagami, T. (2006). Short-term annealing characteristics of spontaneous fission tracks in zircon: A qualitative description. Chemical Geology, 227(3–4), 214–222. https://doi.org/10.1016/j.chemgeo.2005.10.002
- Nasdala, L., Irmer, G., & Wolf, D. (1995). The degree of metamictization in zircon: A Raman spectroscopic study. European Journal of Mineralogy, 471–478. https://doi.org/10.1127/ejm/7/3/0471
- Nasdala, L., Reiners, P. W., Garver, J. I., Kennedy, A. K., Stern, R. A., Balan, E., & Wirth, R. (2004). Incomplete retention of radiation damage in zircon from Sri Lanka. *American Mineralogist*, 89(1), 219–231. https://doi.org/10.2138/am-2004-0126
- Nuriel, P., Miller, D. M., Schmidt, K. M., Coble, M. A., & Maher, K. (2019). Ten-million years of activity within the Eastern California Shear Zone from U–Pb dating of fault-zone opal. *Earth and Planetary Science Letters*, 521, 37–45. https://doi.org/10.1016/j.epsl.2019.05.047
- Nuriel, P., Rosenbaum, G., Zhao, J.-X., Feng, Y., Golding, S. D., Villemant, B., & Weinberger, R. (2012). U-Th dating of striated fault planes. Geology, 40(7), 647–650. https://doi.org/10.1130/g32970.1
- Orme, D. A., Guenthner, W. R., Laskowski, A. K., & Reiners, P. W. (2016). Long-term tectonothermal history of Laramide basement from zircon–He age-eU correlations. *Earth and Planetary Science Letters*, 453, 119–130. https://doi.org/10.1016/j.epsl.2016.07.046
- Peters, K. E., Walters, C. C., & Moldowan, J. M. (2007). The biomarker guide: Volume 2, Biomarkers and isotopes in petroleum systems and earth history. Cambridge University Press.
- Platt, J. D., Brantut, N., & Rice, J. R. (2015). Strain localization driven by thermal decomposition during seismic shear. *Journal of Geophysical Research: Solid Earth*, 120(6), 4405–4433. https://doi.org/10.1002/2014ib011493
- Platt, J. D., Rudnicki, J. W., & Rice, J. R. (2014). Stability and localization of rapid shear in fluid-saturated Fault gouge: 2. Localized zone width and strength evolution. *Journal of Geophysical Research: Solid Earth*, 119(5), 4334–4359. https://doi.org/10.1002/2013jb010711
- Polissar, P. J., Savage, H. M., & Brodsky, E. E. (2011). Extractable organic material in fault zones as a tool to investigate frictional stress. Earth and Planetary Science Letters, 311(3-4), 439–447. https://doi.org/10.1016/j.epsl.2011.09.004
- Powell, J., Schneider, D., Stockli, D., & Fallas, K. (2016). Zircon (U-Th)/He thermochronology of Neoproterozoic strata from the Mackenzie Mountains, Canada: Implications for the Phanerozoic exhumation and deformation history of the northern Canadian Cordillera. *Tectonics*, 35(3), 663–689. https://doi.org/10.1002/2015tc003989
- Rabinowitz, H., Polissar, P., & Savage, H. (2017). Reaction kinetics of alkenone and n-alkane thermal alteration at seismic timescales. *Geochemistry, Geophysics, Geosystems*, 18(1), 204–219. https://doi.org/10.1002/2016gc006553
- Radke, M. (1988). Application of aromatic compounds as maturity indicators in source rocks and crude oils. *Marine and Petroleum Geology*, 5(3), 224–236. https://doi.org/10.1016/0264-8172(88)90003-7
- Reches, Z. e., & Lockner, D. A. (2010). Fault weakening and earthquake instability by powder lubrication. *Nature*, 467(7314), 452–455. https://doi.org/10.1038/nature09348
- Reiners, P. W. (2005). Zircon (U-Th)/He thermochronometry. Reviews in Mineralogy and Geochemistry, 58(1), 151–179. https://doi.org/10.2138/rmg.2005.58.6
- Reiners, P. W. (2009). Nonmonotonic thermal histories and contrasting kinetics of multiple thermochronometers. *Geochimica et Cosmochimica Acta*, 73(12), 3612–3629. https://doi.org/10.1016/j.gca.2009.03.038
- Reiners, P. W., Spell, T. L., Nicolescu, S., & Zanetti, K. A. (2004). Zircon (U-Th)/He thermochronology: He diffusion and comparisons with <sup>40</sup>Ar/<sup>39</sup>Ar dating. *Geochimica et Cosmochimica Acta*, 68, 1857–1887. https://doi.org/10.1016/j.gca.2003.10.021
- Rice, J. R. (2006). Heating and weakening of faults during earthquake slip. *Journal of Geophysical Research*, 111(B5), B05311. https://doi.org/10.1029/2005jb004006
- Rice, J. R., Rudnicki, J. W., & Platt, J. D. (2014). Stability and localization of rapid shear in fluid-saturated Fault gouge: 1. Linearized stability analysis. *Journal of Geophysical Research: Solid Earth*, 119(5), 4311–4333. https://doi.org/10.1002/2013jb010710
- Rowe, C. D., & Griffith, W. A. (2015). Do faults preserve a record of seismic slip: A second opinion. *Journal of Structural Geology*, 78, 1–26. https://doi.org/10.1016/j.jsg.2015.06.006
- Savage, H. M., & Polissar, P. J. (2019). Biomarker thermal maturity reveals localized temperature rise from paleoseismic slip along the Punch-bowl Fault, CA, USA. Geochemistry, Geophysics, Geosystems, 20(7), 3201–3215. https://doi.org/10.1029/2019gc008225
- Savage, H. M., Polissar, P. J., Sheppard, R., Rowe, C. D., & Brodsky, E. E. (2014). Biomarkers heat up during earthquakes: New evidence of seismic slip in the rock record. *Geology*, 42(2), 99–102, https://doi.org/10.1130/g34901.1
- Savage, H. M., Rabinowitz, H. S., Spagnuolo, E., Aretusini, S., Polissar, P. J., & Di Toro, G. (2018). Biomarker thermal maturity experiments at earthquake slip rates. Earth and Planetary Science Letters, 502, 253–261. https://doi.org/10.1016/j.epsl.2018.08.038
- Schulz, S. E., & Evans, J. P. (1998). Spatial variability in microscopic deformation and composition of the Punchbowl fault, southern California: Implications for mechanisms, fluid-rock interaction, and fault morphology. *Tectonophysics*, 295(1–2), 223–244. https://doi.org/10.1016/s0040-1951(98)00122-x
- Schulz, S. E., & Evans, J. P. (2000). Mesoscopic structure of the Punchbowl Fault, Southern California and the geologic and geophysical structure of active strike-slip faults. *Journal of Structural Geology*, 22(7), 913–930. https://doi.org/10.1016/s0191-8141(00)00019-5
- Sheppard, R., Polissar, P., & Savage, H. (2012). Rapid heating experiments demonstrate the usefulness of organic molecules as an earthquake thermometer (pp. T13B–T2603). AGUFM.
- Sheppard, R. E., Polissar, P. J., & Savage, H. M. (2015). Organic thermal maturity as a proxy for frictional fault heating: Experimental constraints on methylphenanthrene kinetics at earthquake timescales. *Geochimica et Cosmochimica Acta*, 151, 103–116. https://doi.org/10.1016/j.gca.2014.11.020

ARMSTRONG ET AL. 19 of 20



- Shuster, D. L., Flowers, R. M., & Farley, K. A. (2006). The influence of natural radiation damage on helium diffusion kinetics in apatite. *Earth and Planetary Science Letters*, 249, 148–161.
- Tagami, T. (2012). Thermochronological investigation of fault zones. *Tectonophysics*, 538, 67–85. https://doi.org/10.1016/j.tecto.2012.01.032 van der Pluijm, B. A., Hall, C. M., Vrolijk, P. J., Pevear, D. R., & Covey, M. C. (2001). The dating of shallow faults in the Earth's crust. *Nature*, 412(6843), 172–175. https://doi.org/10.1038/35084053
- Wibberley, C. A., & Shimamoto, T. (2005). Earthquake slip weakening and asperities explained by thermal pressurization. *Nature*, 436(7051), 689–692. https://doi.org/10.1038/nature03901
- Wilson, J., Chester, J., & Chester, F. (2003). Microfracture analysis of fault growth and wear processes, Punchbowl Fault, San Andreas system, California. *Journal of Structural Geology*, 25(11), 1855–1873. https://doi.org/10.1016/s0191-8141(03)00036-1
- Woodburne, M. O. (1975). Cenozoic Stratigraphy of the Transverse Ranges and Adjacent Areas, Southern California (Vol. 162). Geological Society of America.
- Woodhead, J. A., Rossman, G. R., & Silver, L. T. (1991). The metamictization of zircon: Radiation dose-dependent structural characteristics. American Mineralogist, 76(1-2), 74-82.

# **References From the Supporting Information**

- Bostick, N., Cashman, S., McCulloh, T., & Waddell, C. (1978). Gradients of vitrinite reflectance and present temperature in the Los Angeles and Ventura basins. California.
- Cardwell, R., Chinn, D., Moore, G., & Turcotte, D. (1978). Frictional heating on a fault zone with finite thickness. Geophysical Journal International, 52(3), 525–530.
- Carlson, W. D., Donelick, R. A., & Ketcham, R. A. (1999). Variability of apatite fission-track annealing kinetics: I. Experimental results. American Mineralogist, 84(9), 1213–1223. https://doi.org/10.2138/am-1999-0901
- Donelick, R. A., O'Sullivan, P. B., & Ketcham, R. A. (2005). Apatite fission-track analysis. *Reviews in Mineralogy and Geochemistry*, 58(1), 49–94. https://doi.org/10.2138/rmg.2005.58.3
- Farley, K. A., Wolf, L. T., & Silver, L. T. (1996). The effects of long alpha-stopping distances on (U-Th)/He ages. *Geochimica et Cosmochimica Acta*, 60, 4223–4229. https://doi.org/10.1016/S0016-7037(96)00193-7
- Farley, K. A., Rusmore, M. E., & Bogue, S. W. (2001). Post-10 Ma uplift and exhumation of the northern Coast Mountains, British Columbia. Geology, 29(2), 99–102. https://doi.org/10.1130/0091-7613(2001)029<0099:PMUAEO>2.0.CO;2
- Gleadow, A. J. W. (1981). Fission-track dating methods: What are the real alternatives? *Nuclear Tracks*, 5, 3–14. https://doi.org/10.1016/0191-278X(81)90021-4
- Gleadow, A. J., Belton, D. X., Kohn, B. P., & Brown, R. W. (2002). Fission track dating of phosphate minerals and the thermochronology of apatite. Reviews in Mineralogy and Geochemistry, 48(1), 579–630. https://doi.org/10.2138/rmg.2002.48.16
- Hourigan, J. K., Reiners, P. W., & Brandon, M. T. (2005). U-Th zonation-dependent alpha-ejection in (U-Th)/He chronometry. *Geochimica et Cosmochimica Acta*, 69(13), 3349–3365. https://doi.org/10.1016/j.gca.2005.01.024

ARMSTRONG ET AL. 20 of 20